RESEARCH ARTICLE

Surface heat budget in the Southern Ocean from 42°S to the Antarctic marginal ice zone: four atmospheric reanalyses versus icebreaker *Aurora Australis* measurements

Lisan Yu[1], Xiangze Jin[1] & Eric W. Schulz[2]

[1] Department of Physical Oceanography, Woods Hole Oceanographic Institution, Woods Hole, MA, USA;
[2] Centre for Australian Weather and Climate Research, Australian Bureau of Meteorology, Melbourne, Victoria, Australia

Abstract

Surface heat fluxes from four atmospheric reanalyses in the Southern Ocean are evaluated using air–sea measurements obtained from the *Aurora Australis* during off-winter seasons in 2010–12. The icebreaker tracked between Hobart, Tasmania (ca. 42°S), and the Antarctic continent, providing in situ benchmarks for the surface energy budget change in the Subantarctic Southern Ocean (58–42°S) and the eastern Antarctic marginal ice zone (MIZ, 68–58°S). We find that the reanalyses show a high-level agreement among themselves, but this agreement reflects a universal bias, not a "truth." Downward shortwave radiation (SW↓) is overestimated (warm biased) and downward longwave radiation (LW↓) is underestimated (cold biased), an indication that the cloud amount in all models is too low. The ocean surface in both regimes shows a heat gain from the atmosphere when averaged over the seven months (October–April). However, the ocean heat gain in reanalyses is overestimated by 10–36 W m^{-2} (80–220%) in the MIZ but underestimated by 6–20 W m^{-2} (7–25%) in the Subantarctic. The biases in SW↓ and LW↓ cancel out each other in the MIZ, causing the surface heat budget to be dictated by the underestimation bias in sensible heat loss. These reanalyses biases affect the surface energy budget in the Southern Ocean by meaningfully affecting the timing of the seasonal transition from net heat gain to net heat loss at the surface and the relative strength of SW↓ at different regimes in summer, when the length-of-day effect can lead to increased SW↓ at high latitudes.

Keywords

Surface fluxes; surface energy budget; overestimation bias; underestimation bias; surface meteorology; icebreaker-based meteorological measurements

Correspondence

Lisan Yu, Department of Physical Oceanography, Mail Stop #21, Woods Hole Oceanographic Institution, Woods Hole, MA 02543, USA. E-mail: lyu@whoi.edu

Abbreviations

ACC: Antarctic Circumpolar Current; CFSR: National Centers for Environmental Prediction Climate Forecast System Reanalysis; COARE: Coupled Ocean–Atmosphere Response Experiment; ERA-interim: European Centre for Medium-Range Weather Forecasts Interim Reanalysis; K: Kelvin degrees; LH: latent heat; LW: longwave radiation (LW↓: downward LW; LW↑: upward LW); MERRA: National Aeronautical and Space Administration Modern Era Reanalysis for Research and Applications; MIZ: marginal ice zone; NCEP1: National Centers for Environmental Prediction/ National Center for Atmospheric Research Reanalysis 1; NSIDC: US National Sea Ice Data Center; OSTIA: Operational Sea Surface Temperature and Sea Ice Analysis; RMS: root mean square; SIC: sea-ice concentration; SH: sensible heat; SHEBA: Surface Heat Budget of the Arctic Ocean project; SD: standard deviation; SW: shortwave radiation (SW↓: downward SW; SW↑: upward SW)

Introduction

The Southern Ocean poleward of 42°S (Hobart, Australia) features two important air–sea interaction regimes: the strong wind regime that is associated with the ACC, and the significant MIZ that girdles the northern edge of the Antarctic pack ice. The annual advance and retreat of Antarctic sea ice create a vast sea-ice transition zone that covers ca. 16 million km^2 (Wadhams et al. 1986; Allison et al. 1993; Zwally et al. 2002), which is equivalent to twice the size of Australia. The transition from full sea-ice coverage to a generally ice-free zone produces one of

Citation: *Polar Research* 2019, *38*, 3349, http://dx.doi.org/10.33265/polar.v38.3349

the largest annual albedo variations in the global ocean, and opens the door to complex feedbacks and interactions between the atmosphere, sea ice and open ocean (e.g., Bromwich et al. 1998; Yuan & Martinson 2000; Hudson & Hewitson 2001).

Sea ice modulates air–sea radiative and turbulent heat exchanges in addition to the thermodynamic properties of the surface. The co-existence of ice and open water in the MIZ creates strong cross-margin gradients in albedo, temperature and roughness (Andreas et al. 1984; Bennett & Hunkins 1986; McPhee et al. 1987; Ruffieux et al. 1995; Brandt et al. 2005). Over the open water, surface albedo is typically low, around 0.055. In the sea-ice domain, albedo is so sensitive to the changes of sea state, solar elevation and cloudiness that its value increases from 0.12 to 0.20 for a non-snow-covered very thin ice surface up to 0.87 for thick snow-covered ice under cloud (Allison et al. 1982; Brandt et al. 2005). The highly variable nature of surface albedo suggests that a change of open water area in the ice margin, even if small, can affect the amount of solar radiation input and set off the positive ice-albedo feedback that further amplifies initial perturbations (e.g., Manabe & Stouffer 1980; Tetzla et al. 2015). In addition, sea ice is a natural insulator that keeps the water thermally inactive under the ice/snow covers. When a lead opens up, the sharp air–sea thermal contrast can drive enormous turbulent heat fluxes over the exposed surface water, causing SH flux to exceed 400 W m^{-2} and LH flux to go beyond 130 W m^{-2} (Andreas et al. 1979; McPhee et al. 1987; Kottmeier & Engelbart 1992). The heat released to the atmospheric modifies the thermodynamic processes in the atmospheric boundary layer (Alam & Curry 1995; Nygard et al. 2016), and energies localized convection above and downwind of the lead. Schnell et al. (1989) observed plumes of ice crystals emanating from a wide lead that reached up to 4 km height and were traced 250 km in the direction that the winds were blowing.

Accurate quantification of the surface heat budget from the ACC to the Antarctic MIZ is important because the Antarctic region south of the ACC loses a substantial amount of heat to the overlying atmosphere by as much as 0.2–0.65 PW (1 PW = 10^{15} W) on an annual mean basis (e.g., Hastenrath 1982). Heat loss at high latitudes must be balanced by a compensating ocean poleward heat transport from low latitudes. Yet, unlike the Northern Hemisphere, where ocean currents transport heat directly to the ice margin to about 70°N, the poleward heat transport in the Southern Ocean is restricted by the near-zonal flow of the ACC that encircles the Antarctic Continent (Rintoul et al. 2001). It remains to be known whether eddies or mean currents are the main vehicle for the ocean heat transport southward across the ACC (e.g., Cerovečki et al. 2011). An improved estimation of the surface heat budget at the high-latitude Southern Ocean will certainly help to better characterize the contribution of various ocean processes to poleward heat transport.

The Southern Ocean is the most challenging place to observe. In situ observations in the periphery of the MIZ—defined by the SIC greater than 15% (Comiso & Zwally 1984)—are hard to obtain (King & Turner 1997; Schulz et al. 2012). While satellite passive microwave sensors and scatterometers are a powerful platform for measuring air–sea variables over the ice-free open oceans, signal contamination makes them unreliable near the ice edge (e.g., signal mixtures of open water and thin or pack ice). One plausible approach to construct air–sea flux estimates in the MIZ is to merge satellite open-ocean observations with atmospheric reanalysis (e.g., Yu & Weller 2007). Such approach requires a good knowledge of the performance of atmospheric reanalysed surface fluxes both in the ACC regime and under sea-ice conditions. Because in situ observations in these regions are rare, evaluation of the South Ocean fluxes has been available at only a few locations (e.g., Kottmeier & Sellmann 1996; McPhee et al. 1996; Vihma et al. 2002; Wendler et al. 2005). There are relatively more in situ measurements of the Arctic fluxes (e.g., Andreas et al. 1979; Bennett & Hunkins 1986; Ruffieux et al. 1995; Renfrew et al. 2002; Wilson et al. 2002; Grachev et al. 2007; Tetzla et al. 2015; Walden et al. 2017; Grachev et al. 2018).

The icebreaker *Aurora Australis* is a research and supply vessel running between Hobart, Tasmania (ca. 42°S), and three permanent research stations—Casey, Davis and Mawson—on the Antarctic continent during the off-winter months. Automated meteorological measurement systems are deployed onboard the vessel so that measurements of surface flux-related variables, including wind, air and sea temperature, humidity, pressure, precipitation, LW↓ and SW↓, are recorded routinely. Yu et al. (2017) processed the icebreaker's measurements between December 2010 and April 2012, and showed that the shipboard measurements provide valuable in situ insights into the air–sea heat exchange processes in the ACC and MIZ. The most marked feature is the significant seasonal changes of turbulent LH and SH fluxes in the Antarctic ice margin when compared to those in the Subantarctic open ocean. The sharp increase of LH and SH fluxes during the transition from late summer to fall turned the MIZ quickly into a heat loss regime. The turbulent fluxes in the ACC region showed relatively weaker seasonal variations, and the open water was mostly a heat-gain region during the off-winter seasons.

Balancing surface heat budget remains a challenging issue (e.g., Wilson et al. 2002; Serreze & Barry 2005;

Citation: *Polar Research* 2019, *38*, 3349, http://dx.doi.org/10.33265/polar.v38.3349

Foken 2008; Jacobs et al. 2008; Leuning et al. 2012) because the net budget is a small residual between the several large heat exchange processes, including SW↓, SW↑, LW↑, LW↓, turbulent LH and SH latent and heat transfers. Some of the exchanges (e.g., SW↓ and LW↓) are observable, but most exchanges are parameterized using air–sea variables that can be observed and/or modelled. The parameterized flux estimates usually have uncertainties, and the latter may accumulate and present obstacles to the balance of surface heat budget using either satellite products or atmospheric reanalysis fluxes (e.g., Walden et al. 2017; Yu 2019). The surface meteorological measurements from the icebreaker *Aurora Australis* provide a rare opportunity to evaluate the flux products and to understand how the heat budget changes in the remote Southern Ocean. This study aims to take advantage of the analysis of Yu et al. (2017) and use the derived ship-based fluxes as a reference to examine the performance of atmospheric reanalysis flux products in the ship-tracked region. Satellite products are not included because the lack of satellite retrievals makes it unfeasible to use these products to estimate the heat exchanges in the MIZ.

The presentation of this study is organized as follows. The following section provides a description of shipboard air–sea measurements and fluxes. The air–sea heat fluxes from four gridded reanalysis products are characterized and compared statistically with the ship-based measurements. The leading uncertainties in computing surface heat budget with and without the influence of ice are then addressed. The final section comprises a summary and conclusions.

Shipboard measurements

Data processing

This study uses measurements obtained between December 2010 and April 2012 from 10 round-trips (20 ship tracks) between Hobart and the Antarctic continent (Table 1, Fig. 1a). The measured meteorological and oceanographic variables include sea surface temperature, wind speed and direction, air temperature, relative humidity, air pressure, LW↓ and SW↓ (Table 2). During voyages of this ship, observations are fed into the existing ship data management system that creates one-min averages of surface meteorological observations. These data files are broadcasted via satellite back to Australia every 30 min. Data quality control and the computation of a five-min averaged bulk flux based on the COARE formulation (Fairall et al. 2003) are performed at the Australia Bureau of Meteorology as part of the Australian Integrated Marine Observing System (Meyers 2008; Hill 2010).

Table 1 List of the 10 round-trip cruises between Hobart, Australia, and the Antarctic continent.

Cruises	Start date	End date	Duration	Obs. days
1	02/12/10	31/12/10	30	30
2	04/01/11	06/02/11	34	30
3	07/02/11	17/03/11	39	36
4	18/03/11	18/04/11	32	32
5	20/04/11	05/05/11	16	16
6	14/10/11	30/11/11	48	47
7	02/12/11	31/12/11	30	29
8	02/01/12	15/03/12	74	70
9	17/03/12	14/04/12	29	29
10	15/04/12	01/05/12	17	17

The surface meteorological measurement system includes dual sensors for relative humidity, near-surface air potential temperature, SW↓ and LW↓ on port and starboard, and one wind sensor on the main mast. The quality control procedures identify suspect observations and select observations to use in the bulk turbulent heat flux calculations. Specifically, humidity and temperature measurements are flagged if they exceed physical limits. The computation of the five-min bulk fluxes uses the wind from forward of the beam and the upwind humidity and temperature. The one-min SW↓ measurement is the highest value of the sensor pair (the lower value is more likely to be shaded by the superstructure), while the one-min LW↓ measurement is based on the mean of the sensor pair. These quality control steps are designed to minimize the impact of the ship on the surface meteorological measurements and fluxes. Testing of the quality control procedures was performed for the Integrated Marine Observing System research vessel *Southern Surveyor* using a moored buoy at the Southern Ocean Flux Station (142.0°E, 46.8°S), where the ship and buoy were co-located for 23 hr. The inter-calibration showed that the 10-m neutral wind has a bias of −0.9 m s^{-1} (RMS 1.1 m s^{-1}), SW↓ 3 W m^{-2} (RMS 42 W m^{-2}), LW↓ −0.3 W m^{-2} (RMS 11 W m^{-2}), SH −1 W m^{-2} (RMS 9 W m^{-2}) and LH −5 W m^{-2} (RMS 12 W m^{-2}) (Schulz et al. 2012).

Reprocessing the shipboard measurements for research purposes was conducted by Yu et al. (2017). The reprocessing had three main objectives, as follows. The first was to construct daily mean time series. Hourly time series were first obtained by averaging one-min measurements. For each day, SW↓ hourly means were checked to see whether they were able to depict a full diurnal cycle. If the diurnal peak values were missing, the data were deemed insufficient to depict a full diurnal cycle. The data for that particular day were then eliminated to minimize the aliasing due to uneven sampling. The second objective was to bin daily mean data points onto one-degree

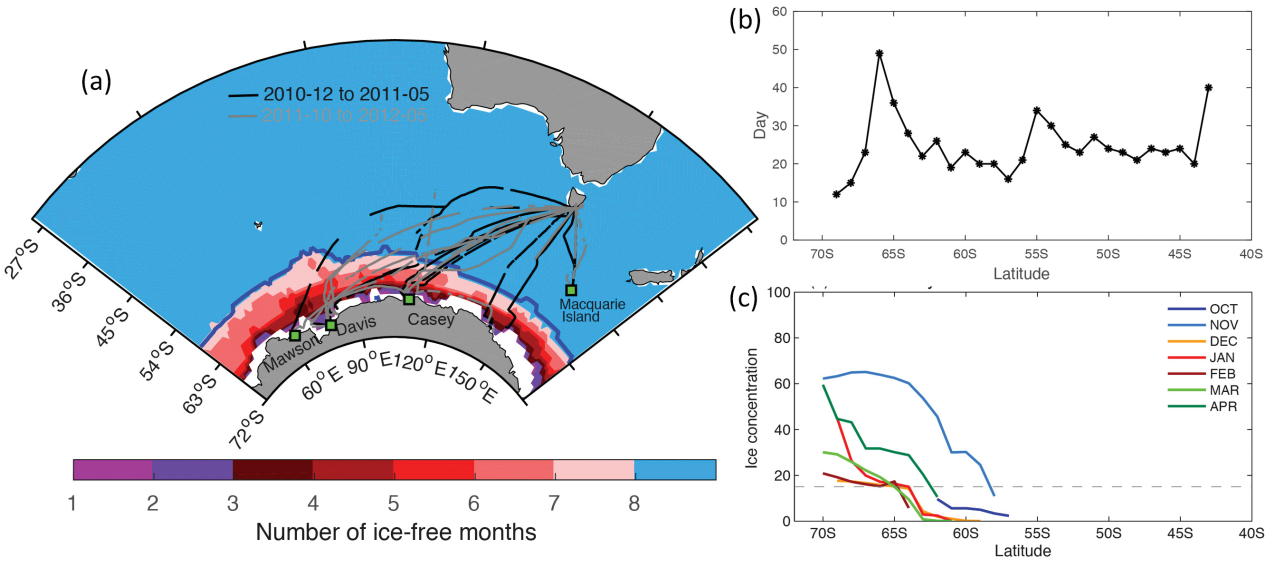

Fig. 1 (a) The ship routes between Hobart, Australia, and the Antarctic continent. The blue line denotes the equatorward edge of the MIZ. (b) Number of observations constructed from all available measurements along the ship's tracks, and (c) monthly mean condition of the SIC with the 15% SIC denoted by the dashed black line.

Table 2 List of the shipboard measurements and the height of the measurements.

Observation	Instrument	Location	Height above water (m)
Wind speed and direction	RM Young 05106	Main mast	31
Air temperature	2 × Vaisala HMT33	Main mast, cross-tree, port and starboard	20
Relative humidity	2 × Vaisala HMT33	Main mast, cross-tree, port and starboard	20
Air pressure	Vaisala PTB220	Bridge	16
Water temperature	Seabird SBE 38	Water intake	-5
Longwave radiation	2 × Eppley PIR	Above bridge, port and starboard	18.5
Shortwave radiation	Middleton EQ08 Solar Pyranometer	Above bridge, port and starboard	18.5

grids along each ship track and group them onto calendar months. Most ship observations were acquired between October and April (austral off-winter seasons). Only a few observations occurred in May, and no observations during June–September (austral winter). The number of total useful measurement days during the seven months on each one-degree binned grid is shown in Fig. 1b. The third main objective was to determine the cut-off latitude for the seasonal MIZ. The MIZ is defined by the SIC in the range of 15% (the sparse ice) to 85% (the pack ice), following Strong & Rigor (2013). As the ship data reports include no sea-ice observations, SIC data from the NSIDC were used to estimate the outer edge (15% SIC) of the MIZ along each ship track. The Antarctic ice in the MIZ is mostly seasonal ice. During the seven months (October–April), the outer edge of the MIZ retreated from the seasonal maximum extension at roughly 58°S in October all the way to the coast off the Antarctic continent in February (Fig. 1c). The region encircled by the northernmost edge of the 15% SIC (i.e., the blue line in Fig. 1) is referred to as the seasonal MIZ. Note that the Mercator map projections exaggerate the areal significance at high latitudes relative to low latitudes. Our study region has a meridional extent from 42°S to 68°S, within which the seasonal MIZ can be separated from the Subantarctic open ocean at 58°S. Using a sector bounded by 40–170°E, the MIZ region has an area of 3×10^6 km^2, covering 26% of the study region. A 1° ×1° region near the ice edge (at 68°S) represents an area just over half (58%) the size of a 1° ×1° region in the middle of the Subantarctic (at 50°S).

The separation latitude of 58°S is the latitude that separates the permanent ice-free regime (defined as the Subantarctic Southern Ocean) from the Antarctic MIZ that is influenced by seasonal ice. This distinction allows

Citation: *Polar Research* 2019, *38*, 3349, http://dx.doi.org/10.33265/polar.v38.3349

the examination of the seasonal variations of surface heat budget with and without the influence of ice, but it is not the cut-off latitude of the MIZ for each track. Along the ship track, whether individual observations should be regarded as Subantarctic or MIZ was determined by the coincident SIC observations at the time of the observation.

Computation of the ship-based fluxes over the MIZ and the open water

The sea surface turbulent LH and SH fluxes as well as SW and LW along the ship's tracks were computed from the flux parameterizations using hourly averaged surface meteorological conditions measured at sea. Because sea ice modulates the dynamic and thermodynamic properties of the surface and affects air–sea radiative and turbulent heat exchanges, the flux algorithm for the open ocean differs from that used for the MIZ. The algorithms used in the study are described below.

The permanent ice-free Subantarctic ocean. Over the ice-free Subantarctic ocean, LH and SH were computed using the COARE formulae (Fairall et al. 2003):

$$\mathrm{LH} = \rho\, L_e\, c_e\, W\, (q_s - q_a(rh)) \quad (1)$$

$$\mathrm{SH} = \rho\, c_p\, c_h\, W\, (T_s - T_a), \quad (2)$$

where ρ is the density of air, L_e is the LH of evaporation, c_p is the specific heat capacity of air at constant pressure and W is the wind speed at 10-m height. The coefficients c_e and c_h are turbulent transfer coefficients for LH and SH, respectively, and they are functions of wind speed, height and atmospheric stability. The surface and near-surface atmospheric specific humidities are denoted by q_s and q_a, respectively, while the sea surface skin temperature is represented by T_s and the near surface air potential temperature by T_a. Note that q_s is computed from the saturation humidity, q_{sat}, for pure water at T_s using the following relation, $q_s = 0.98\, q_{sat}\,(T_s)$, where a multiplier factor of 0.98 is used to take into account the reduction in vapour pressure caused by a typical salinity of 34.

The net SW was computed as

$$\mathrm{SW} = \mathrm{SW}{\downarrow}\ (1-\alpha), \quad (3)$$

where SW↓ is incoming solar radiation measured by the icebreaker and defined positive downward (i.e., heat gain at the ocean surface) and α is the surface albedo of open water, set at 0.055 according to Fairall et al. (2003).

The net LW was computed from the following algorithm:

$$\mathrm{LW} = \varepsilon\ (\sigma\, T_s^4 - \mathrm{LW}{\downarrow}), \quad (4)$$

where LW is defined as positive upward (i.e., heat released to the atmosphere from the ocean surface), LW↓ is the incoming LW measured at sea, σ is the Stefan–Boltzmann constant (5.67×10^{-8} W m^{-2} K^{-4}), ε is the effective emissivity of sea surface and set at 0.97 and T_s is the absolute surface temperature expressed in K. Note that T_s should be a skin temperature, which is not equal to the bulk sea surface temperature measured from the ship. We applied the correction of cool skin effects that is embedded in the COARE algorithm (Fairall et al. 2003).

The seasonal MIZ. Antarctic sea ice is thin, single-year sea ice, or young ice. Albedo is low over new ice, and increases as ice thickens (Allison et al. 1993). To take into account the contribution from the mixed ice and water conditions, the albedo in the MIZ was computed as a weighted average of the ice and water (Allison et al. 1993; Brandt et al. 2005):

$$\alpha = \alpha_i\, c_i + \alpha_w\, (1-c_i), \quad (5)$$

where α_i is the ice-only albedo and a function of latitude and seasons. The albedo values were taken from table 5 by Brandt et al. (2005), which are seasonal dependent for cloudy-sky incident irradiance in the Antarctic MIZ. α_w is the albedo of open water, set at 0.055 (Fairall et al. 2003). c_i is the SIC, extracted from the Special Sensor Microwave Imager along each ship track (Fig.1b).

The work of Brandt et al. (2005) was based on extensive collections of ship observed sea-ice albedo and sea-ice type during the period of 1988–2000. Ten thousand observations, separated by a minimum of six nautical miles along voyage tracks, were used to create "ice-only" albedos as a function of latitude for each of five longitudinal sectors around Antarctica and for each of the four seasons. These ice albedos were then combined with 13 years of SIC estimates from satellite passive microwave measurements to obtain the geographical and seasonal variation of average surface albedo. As of today, the climatology presented by Brandt et al. (2005) remains the only comprehensive source of information on surface albedo and its seasonal and geographical variations in the ocean surrounding Antarctica. The climatology has been used as the benchmark in developing the sea-ice albedo scheme for general circulation models (e.g., Pedersen et al. 2009). Brandt et al. (2005) also showed that the main determinant of area-averaged albedo is the SIC, not the ice type (see figures 8–10 in their paper). This parameterization is suitable for this study, as only the SIC information, not the sea-ice type, is provided by satellite observations.

LH and SH in the MIZ were computed from the algorithm developed by SHEBA (Andreas, Horst et al. 2010), in contrast to the open-ocean fluxes that were estimated using the COARE algorithm. The essence of the SHEBA

bulk flux algorithm is the parameterization of two sea-ice effects on the computation of turbulent transfer coefficients for momentum (or the drag coefficient), LH and SH over the mixed ice and water conditions. The SHEBA algorithm includes the effects of form drag caused by the dynamic pressure of ice floe edges and ridges. Form drag (i.e., pressure forces) is a unique aerodynamic feature in the ice margin, created at vertical faces of large ice floes when winds flow across. The form drag adds to the skin drag, boosting turbulent momentum, heat and moisture exchanges in the ice margin (Andreas et al. 1984). The SHEBA algorithm parameterizes the 10-m total drag at neutral stability, c_d, as a second-order polynomial in ice concentration (Andreas, Horst et al. 2010). That is,

$$10^3\, c_d = 1.500 + 2.233\, c_i - 2.333\, c_i^2 \qquad (6)$$

Estimating LH and SH requires the knowledge of how the scalar roughness lengths can be parameterized for wind speed (z_0), temperature (z_T) and humidity (z_Q) and the stability corrections (Andreas 2002; Fairall et al. 2003). The relation between c_d and z_0 at neutral stability is:

$$c_d = \frac{k^2}{\left\{\ln\left(\frac{10}{z_o}\right) - \psi m\left(\frac{10}{L}\right)\right\}^2}, \qquad (7)$$

where k (= 0.40) is the von Kármán constant. The stability correction, ψ_m, is an empirical function of the Obukhov length L. The SHEBA algorithm predicts z_T and z_Q from Andreas's (1987) theoretical model:

$$\ln(z_s/z_0) = b_0 + b_1 \ln R_* + b_2 (\ln R_*)^2, \qquad (8)$$

where $R_* = u_*\, z_0/\nu$ is the roughness Reynolds number, z_s is either z_T or z_Q, u_* is friction velocity and ν is the kinematic viscosity of air. The polynomial coefficients b_0, b_1 and b_2 for z_T and z_Q are tabulated by Andreas (1987, 2002). Using Eqns. 6–8, the neutral-stability transfer coefficients, c_e and c_h, at 10-m reference height can be computed as follows:

$$c_e = \frac{k^2}{\left\{\ln\left(\frac{10}{z_o}\right) - \psi_m\left(\frac{10}{L}\right)\right\}\left\{\ln\left(\frac{10}{z_Q}\right) - \psi_h\left(\frac{10}{L}\right)\right\}} \qquad (9)$$

$$c_h = \frac{k^2}{\left\{\ln\left(\frac{10}{z_o}\right) - \psi_m\left(\frac{10}{L}\right)\right\}\left\{\ln\left(\frac{10}{z_T}\right) - \psi_h\left(\frac{10}{L}\right)\right\}} \qquad (10)$$

The empirical functions for ψ_h and ψ_m in stable stratification developed by Grachev et al. (2007) are incorporated in the SHEBA algorithm. Efforts to relate the drag coefficients to sea-ice topography have been a focus of several other investigations. For instance, a recent study of Lupkes & Gryanik (2015) developed a stability-dependent parameterization of form drag over sea ice. Such parameterization can better account for surface wind over high and low ice concentration and to include near-surface stability effects of floe edges on the heat transfer coefficient. The SHEBA algorithm does not include stability dependence, which may underrepresent the effects of the edge-related turbulence on heat and momentum transfer coefficients.

It is worth mentioning that the SHEBA algorithm was developed with an objective of creating a unified bulk turbulent flux parametrization that is suitable not only for summer sea ice but also for any marginal ice zone. Andreas, Horst et al. (2010) argued that summer sea ice behaves aerodynamically like the MIZ, as both surfaces are a mix of sea ice and water. In developing a unified neutral-stability drag coefficient at a reference height of 10 m, the SHEBA measurements were merged with comparable measurements made in the Antarctic and Arctic MIZ (Andreas et al. 1984; Anderson 1987; Guest & Davidson 1987; Birnbaum & Lupkes 2002). The result showed that the various data sets yield a consistent picture of how the 10-m neutral-stability drag coefficient varies with ice concentration, suggesting that the SHEBA drag formulation should work for any MIZ in addition to the SHEBA test sites in the Arctic summer.

The other feature of the SHEBA algorithm is the implementation of the SIC-weighted averages of the fluxes to represent the fluxes over the mixed sea-ice surfaces (Vihma 1995). This approach is similar to Eqn. 5 in computing the albedo in the MIZ. By doing so, the SHEBA algorithm has the LH of sublimation over ice, in addition to the LH of vaporization over the open water (leads and ponds). Surface temperatures from water and sea ice are needed in the algorithm. While the temperature near the sea surface is measured, the temperature over the sea ice is taken from ERA-interim.

In terms of scope and complexity, the SHEBA algorithm is similarly the COARE algorithm. This facilitates merging the two algorithms when linking the fluxes from the Subantarctic open ocean to the fluxes in the MIZ. Nevertheless, the SHEBA algorithm differs from the COARE 3.0 algorithm in the inclusion of the effect of wave-induced roughness in addition to the sea-ice effects. COARE parameterizes the surface roughness as a function of wave height and wave period for fully developed seas (i.e., the wind-generated waves are as large as they can be under current wind velocity and fetch conditions). The parameterization is presented through the Charnock relation using either observed wave characteristics or

Citation: *Polar Research* 2019, *38*, 3349, http://dx.doi.org/10.33265/polar.v38.3349

assumed open-ocean waves. The SHEBA algorithm does not include the effect of wave-induced roughness. Wave characteristics within the MIZ cannot be represented by open-ocean waves.

Surface heat budget in the Subantarctic and MIZ. The total net heat flux, Q_{net}, is the sum of the four flux terms:

$$Q_{net} = SW–LW–LH–SH, \quad (11)$$

where Q_{net} and SW are defined positive downward (i.e., the ocean surface receives heat from the atmosphere), while LW, LH and SH are positive upward (i.e., the ocean surface losses heat to the atmosphere).

As shown in Fig. 1, the separation latitude of 58°S was used to divide the ship-tracked areas into two regimes: the permanent ice-free Subantarctic regime and the Antarctic MIZ, which has a mix of sea ice and open water. The separation latitude was not the cut-off latitude of the MIZ for each track. Along each ship track, whether individual observations should be regarded as Subantarctic or MIZ was determined by the coincident SIC information at the time of the observation. These individual observations constituted the base for the computation of seasonal variations of surface heat budget in the two regimes. The surface energy budget analysis in this study focuses on examining the seasonal variations of surface radiative and turbulent heat fluxes during the transition from summer to fall. The issues related to annual surface heat budget closure are not discussed because there are only measurements from October to April, missing the important winter season.

The surface heat budget in the polar regions is one of the driving forces of the observed long-term trend in sea-ice cover and thickness (e.g., Serreze & Barry 2005; Foken 2008). An adequate representation of this surface budget in climate models is highly desired but has rarely been achieved because climate models are yet to fully resolve the surface heat exchange processes that are constantly modified by the sea-ice melting and forming through the year. Parameterization of turbulent LH and SH fluxes that are associated with varying surface ice conditions remains a challenging task (e.g., Andreas, Persson et al. 2010). Experimental field measurements made at Arctic terrestrial sites have suggested that there is a lack of surface energy balance closure at land, mainly due to the underestimation of turbulent fluxes by 15–30% when compared to net radiation measurements (e.g., Wilson et al. 2002; Foken 2008; Jacobs et al. 2008; Leuning et al. 2012). The energy budget balance at high latitudes has been less studied observationally. One reason is that most field measurements are made during off-winter seasons (e.g., Wendler et al. 2005; Walden et al. 2017; Yu et al. 2017), which is insufficient to describe one annual cycle of the surface energy budget. The other reason is that the surface energy budget is strongly modulated by ice motion and ocean heat transport (e.g., Maykut & McPhee 1995). Even if there are year-round measurements of surface heat fluxes at one targeted location, the surface energy budget is usually not balanced without inclusion of ice and/or ocean transports.

Surface heat fluxes from atmospheric reanalyses

Four reanalysis products

Surface heat flux products from four atmospheric reanalyses were evaluated in this study: NCEP1 (Kalnay et al. 1996), CFSR (Saha et al. 2000), ERA-interim (Dee et al. 2011) and MERRA (Rienecker et al. 2011). NCEP1 is the first-generation of atmospheric reanalysis, and CFSR, ERA-interim and MERRA are the latest generation. A summary of major characteristics of the four products is provided in Table 2.

The reanalyses in the 2010–12 period were used. To facilitate the comparison, all products were averaged daily and interpolated linearly onto each observation location using the nearest grid box around the measurement site. Daily mean time series were produced along each ship tracks on the one-degree binned grids. Following the same post-processing as used for shipboard measurements, collocated reanalysis fluxes were produced along the ship tracks and grouped onto the corresponding calendar months. In the reanalysis, the near-surface wind speed (W) was set at the 10-m height and air temperature (T_a) and specific humidity (q_a) was at the 2-m height. The ship-measured W, T_a and q_a (Table 2) were height adjusted to the same levels as the reanalysis variables using the COARE algorithm.

Treatment of sea-ice and air–sea fluxes in the MIZ

Sea-ice extent is implemented in all four reanalyses, but in various different ways (Table 3). CFSR is the only reanalysis that has an interactive sea-ice model to produce the sea-ice extent, ice thickness, ice and air temperatures, and other ice-related properties (Saha et al. 2010). The sea-ice model is a modification of the Sea Ice Simulator at the Geophysical Fluid Dynamics Laboratory, which includes three layers, two equal layers of sea ice and one (optional) layer of snow with five categories of sea-ice thickness, and SIC is assimilated into the reanalysis system (Wu & Grumbine 2014). In the model, sea-ice dynamics is based on Hunke & Dukowicz (1997), the ice strength follows that of Hibler (1979) and ice thermodynamics is based on Winton (2000).

Table 3 General characteristics of the four atmospheric reanalyses used in the study.

Reanalysis	ERA-interim	CFSR	MERRA	NCEP1
Period	1979–present	1979–present	1979–present	1948–present
Grid spacing	0.7° × 0.7°	0.5° × 0.5°	0.667° × 0.5°	1.875° × 1.875°
Product temporal resolution	6 hourly	Hourly	3 hourly	6 hourly
Data assimilation method	4-DVAR	3-DVAR	3-DVAR	3-DVAR
Treatment of sea ice	SIC prescribed using the OSTIA analysis	SIC produced by a sea-ice model	SIC prescribed using the weekly Reynolds analysis	No sea-ice grids. SIC exceeding 55% set as 100% or else, set as 0.
Albedo over sea ice	Fixed value	From the sea-ice model	Fixed value	N/A

NCEP1 prescribes the SIC based on passive microwave observations from the Special Sensor Microwave Imager (Markus & Cavalieri 2000) and imposes a 55% cut-off. That is, when a grid has SIC exceeding 55%, it is set as an ice grid. When a grid has SIC less than 55%, it is set as an ocean grid (Kalnay et al. 1996). Strictly speaking, NCEP1 has no MIZ. For ERA-interim, the SIC is based on OSTIA that is produced daily at a resolution of 1/20° (approximately 5 km) (Dee et al. 2011). For MERRA, the SIC is linearly interpolated in time from weekly one-degree resolution Reynolds sea surface temperature analysis fields (Rienecker et al. 2011).

NCEP1 has no sea-ice mixed grids on account of the 55% threshold. The computation of surface heat fluxes is simply dependent on whether the grid is over the ocean or ice. CFSR, ERA-interim and MERRA all have grids representing sea-ice conditions and, hence, there are sea-ice effects on the surface fluxes in the MIZ. For instance, in addition to solar zenith angle, the CFSR surface albedo is parameterized as functions of ice thickness and ice temperature that are produced by its sea-ice model (Saha et al. 2010). The ERA-interim summer and winter albedos over sea ice are prescribed by bare sea-ice albedo and dry-snow albedo, respectively (Dee et al. 2011). The MERRA sea-ice albedo is set at 0.6 (Rienecker et al. 2011). In all models, the computation of SW, LH and SH for the sea-ice mixed grids is based on SIC-weighted average of the fluxes over the ocean and ice grids. Surface roughness due to form drag is, however, not explicitly included in the reanalysed turbulent heat flux computations.

Surface energy budgets

Air–sea interaction regimes

The available icebreaker measurements cover two off-winter periods: October 2010–April 2011 and October 2011–April 2012 (Table 1; Fig. 1). The mean turbulent LH and SH fluxes, surface SW and LW and Q_{net} during the two off-winter periods were constructed for the eastern Subantarctic and Antarctic region bounded by 25–75°S in latitude and 30–180°E in longitude (Fig. 2). The edge of the seasonal MIZ (i.e., 15% SIC), which was extracted from the NSIDC's passive microwave data, was superimposed.

The reanalysed turbulent heat loss (LH+SH) in the austral off-winter seasons was generally weak (<50 W m^{-2}) in the ship-tracked region (Fig. 2a). Net surface radiation (SW–LW) decreased poleward, from ca. 120 W m^{-2} near Hobart down to ca. 60 W m^{-2} in the MIZ (Fig. 2b). In all products, the surface heat budget (Q_{net}) was a net heat input to the ocean, with magnitude of 40–60 W m^{-2} in regions poleward of 42°S (Fig. 2c). Differences between these mean products were quantified by using SD. The SD of mean LH+SH products (Fig. 3a) shows that the products differ (SD > 20 W m^{-2}) most in the frontal regimes, such as the East Australian current, the Leeuwin Current off the west Australian coast and the Agulhas return current at ca. 42°S. The SD of mean SW–LW products (Fig. 3b) shows that the products deviate from each other mostly in the subtropical latitudes north of 42°S, outside of the ship-tracked region. The SD of mean Q_{net} products (Fig. 3c) reflects the combined effect of the SD LH+SH and SD SW–LW. The SD Q_{net} differences along the ship tracks are about 10–15 W m^{-2}. Overall, the four reanalyses agree well with each other on the mean flux patterns in the ship-tracked region.

For each product, the inter-monthly variability during the two off-winter periods in 2010–11 and 2011–12 was defined by the SD of monthly mean LH+SH, SW–LW and Q_{net} (Fig. 4). Except for MERRA, the SD LH+SH from CFSR, ERA-interim and NCEP1 produced a similar SD pattern, indicating that the regions of weak LH+SH mean values were also the regions of weak SD LH+SH, and vice versa. This linear correspondence between mean and SD is barely seen in MERRA, as the magnitude of its SD LH+SH monthly variability is overly weak compared to the other three reanalyses. However, the ship-based

Citation: *Polar Research* 2019, *38*, 3349, http://dx.doi.org/10.33265/polar.v38.3349

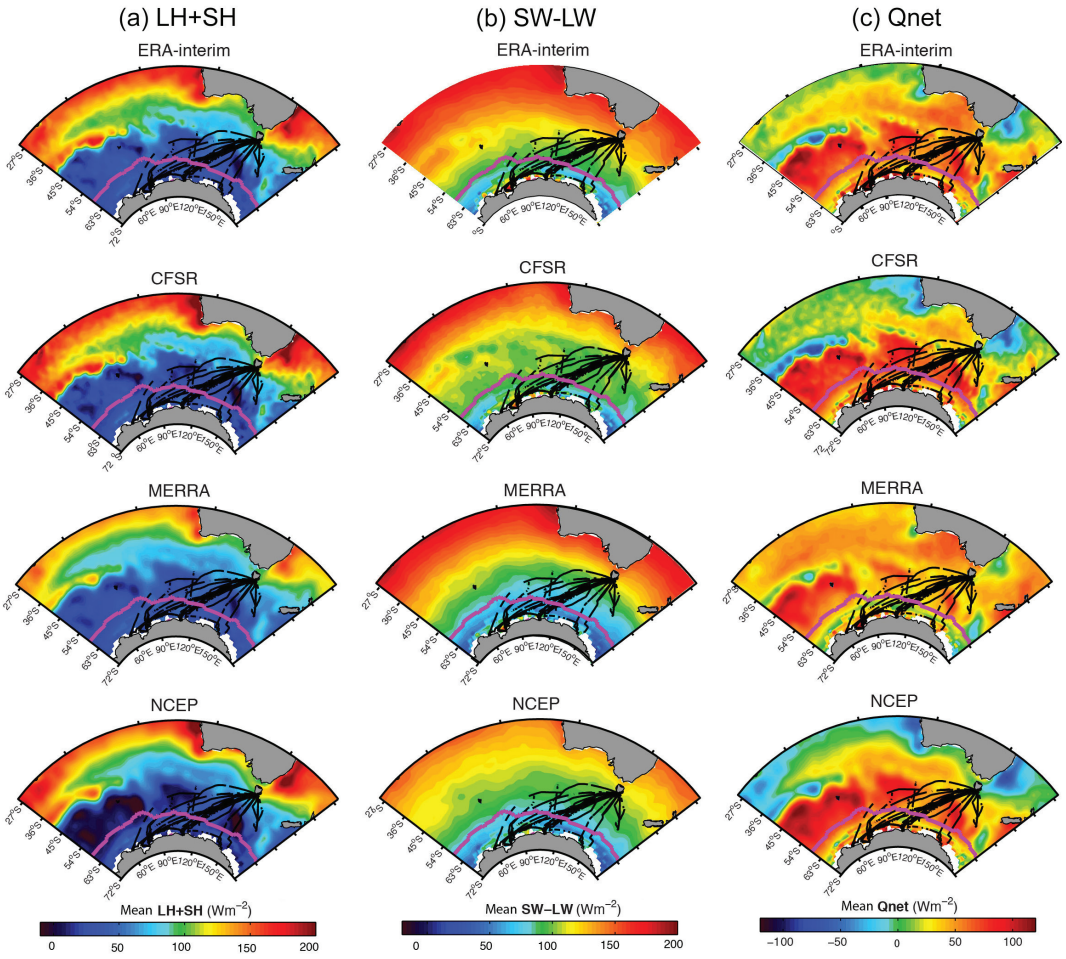

Fig. 2 Seven-month mean fields of (a) LH+SH, (b) SW–LW and (c) Q_{net} constructed from October to April for the two-year period, 2010–11 and 2011–12. The magenta lines at about 60°S denote the location of the seasonal MIZ.

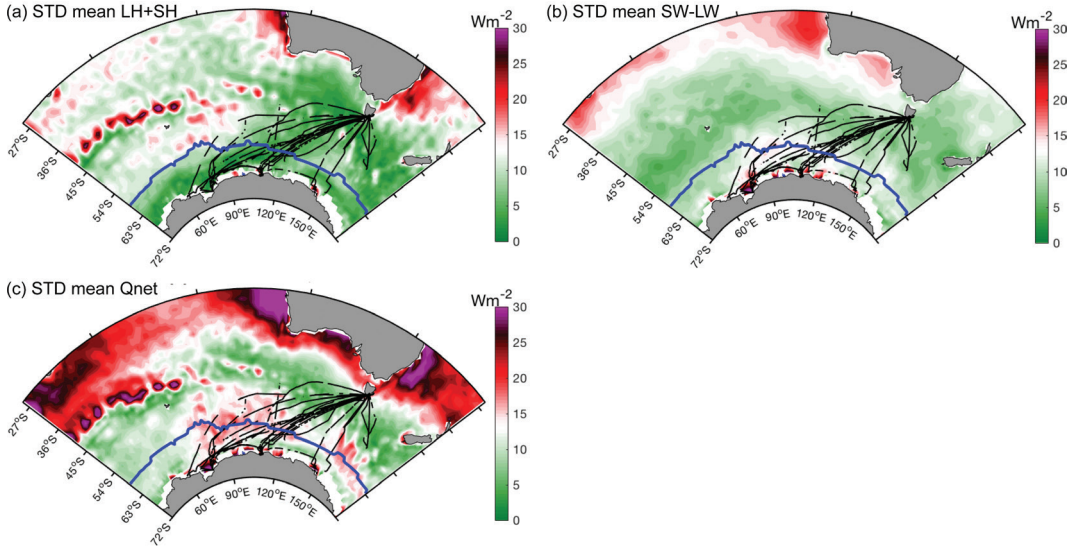

Fig. 3 SD differences between four mean products of (a) LH+SH, (b) SW–LW and (c) Q_{net}. The blue line at about 60°S denotes the location of the seasonal MIZ.

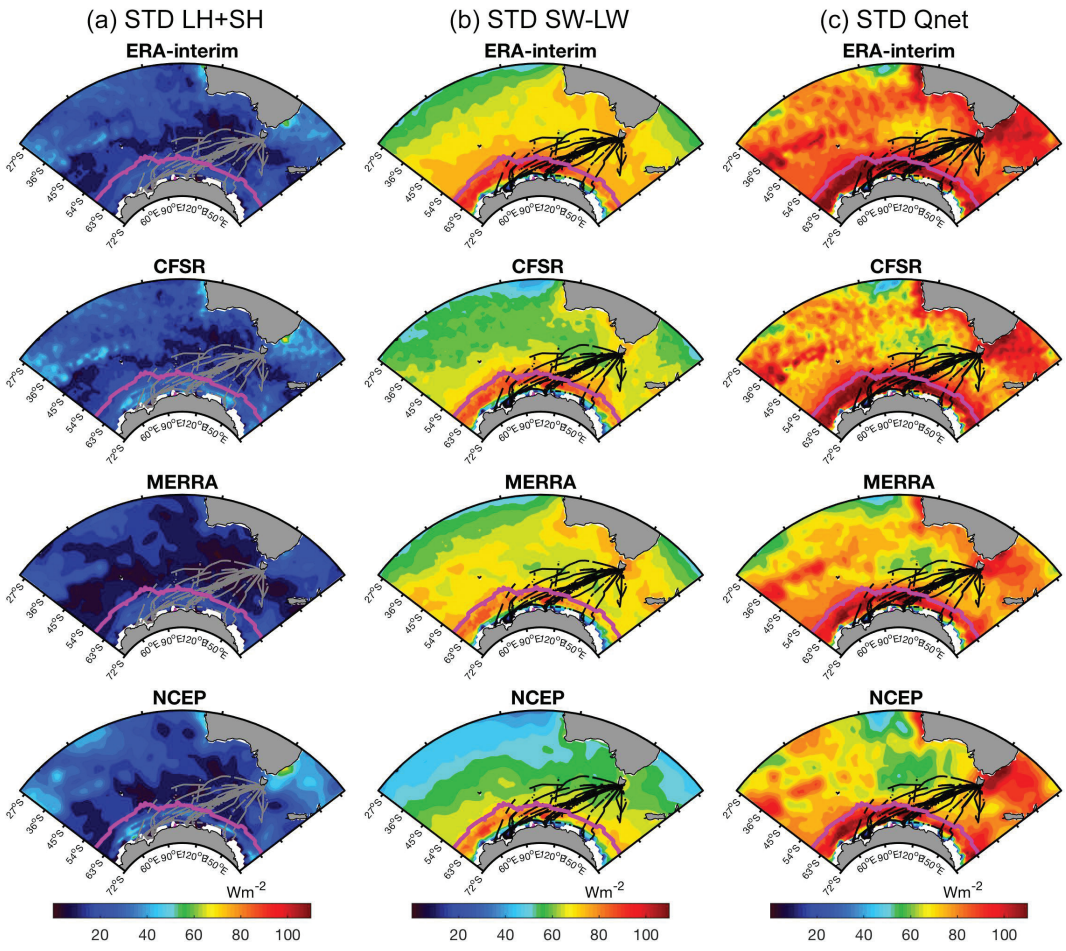

Fig. 4 SD of monthly fields for the seven-month period (October–April) for each product. (a) LH+SH, (b) SW–LW and (c) Q_{net}. The magenta line at about 60°S denotes the location of the seasonal MIZ.

measurements may not have been able to reveal the weakness in MERRA, as SD LH+SH in the ship-tracked region happened to be weak (ca. 10 W m^{-2}) in all products.

The SD SW–LW increased towards the pole, with the maximum SD confined cleanly inside the MIZ (Fig. 4b). While the latitudinal dependence reflects the dominant control of solar elevation angles in seasonal variations of surface radiation budget, the boost of SW–LW variability in the ice margin is an indication of the sea-ice effects on radiative processes. The MIZ-enhanced SW–LW variability clearly dominated the SD Q_{net} pattern in the reanalyses (Fig. 4c). ERA-interim had the largest SD (>100 W m^{-2}) in the MIZ, mostly due to the SW–LW contribution. MERRA and NCEP1 had a similar pattern but a weaker magnitude. CFSR was equally strong as ERA-interim. As mentioned earlier, the four reanalyses treat the ice margin differently. Despite the differences in treating the sea-ice grids, all reanalyses indicated that the sea-ice conditions have major impact on SW–LW variability but limited impact on LH+SH variability.

Air–sea flux variability along the ship track

The icebreaker tracked both the Subantarctic and the MIZ regimes during each of the 10 round trips. Before constructing mean air–sea conditions for the two regimes, the 39-day track during February–March 2011 was selected to examine air–sea variability along the ship track and also to provide a point-to-point comparison of the reanalysis fluxes with ship-based fluxes (Fig. 5). The equatorward edge of the MIZ in February–March and the seven-month maximum equatorward edge of the MIZ were superimposed (Fig. 5a). Both edges were derived from the SIC. The icebreaker left Hobart on 8 February 2011 reached Davis Station, Antarctica, on 1 March and Mawson Station, Antarctica, on 5 March, and returned to Hobart

Citation: *Polar Research* 2019, *38*, 3349, http://dx.doi.org/10.33265/polar.v38.3349

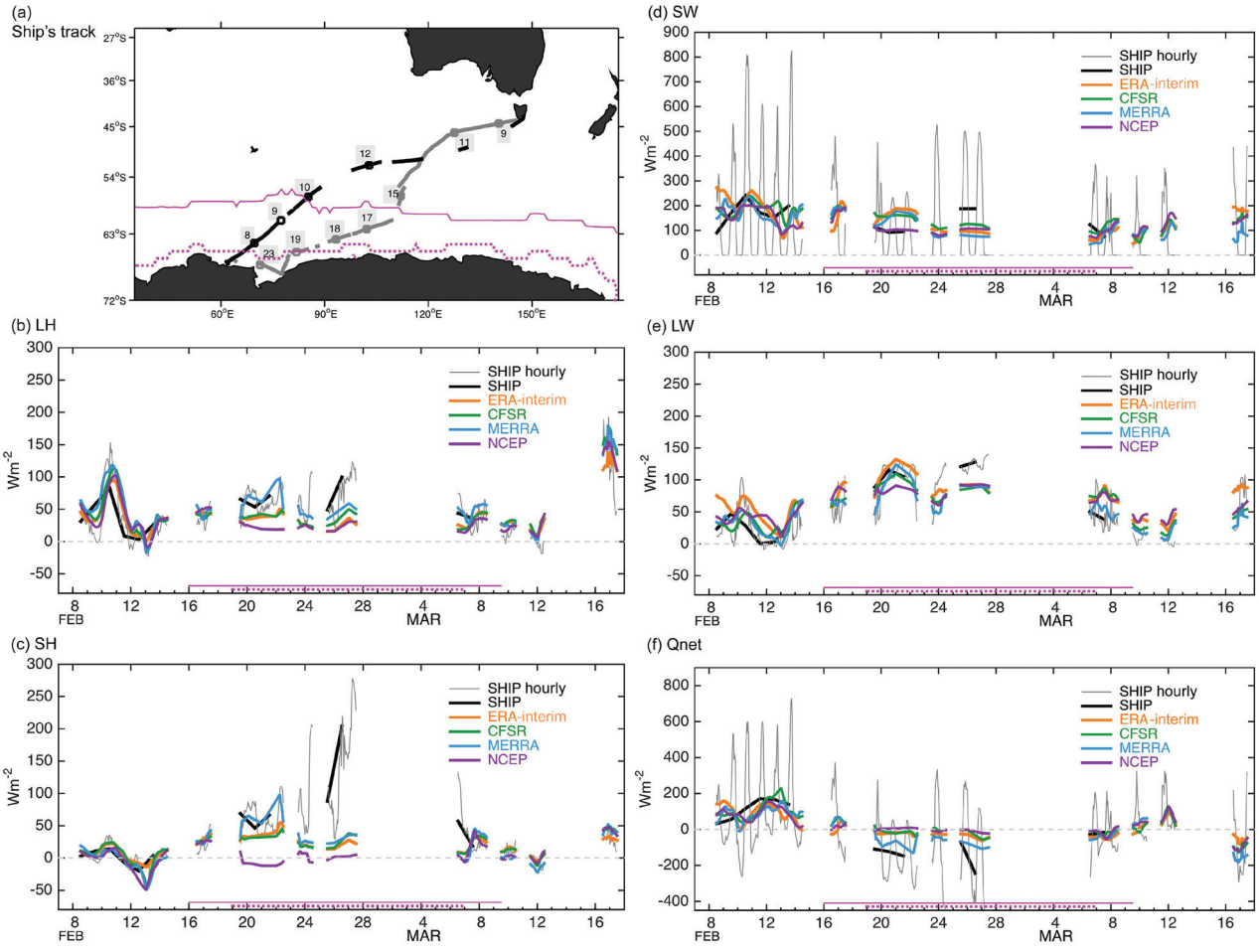

Fig. 5 (a) The ship route started from Hobart, Australia, on 8 February 2011 and returned on 17 March 2011. The solid magenta line denotes the seven-month maximum MIZ and the dashed line denotes the MIZ in February–March 2011. Daily mean fluxes from ship and reanalyses are shown for (b) LH, (c) SH, (d) SW, (e) LW and (f) Q_{net}. The periods that ship traversed in the seasonal and the February–March MIZ are denoted by solid and dashed magenta lines, respectively, on the *x* axis. Hourly ship-based fluxes (thin grey lines) are superimposed in (b)–(f).

on 17 March. The icebreaker first encountered the seven-month maximum outer edge of the MIZ on 16 February. It then traversed across the zone and encountered the narrow MIZ of February–March on 19 February before reaching Mawson Station. The time that the icebreaker stayed in the two zones is shown in Fig. 5b–f.

To assess the range of sub-daily variability and its effect on daily mean values, both hourly mean and daily mean ship flux time series are shown (Fig. 5b–f). Diurnal variability is evident in SW but not significant in LH, SH and LW. The observed diurnal peak of SW reached up to 800 W m^{-2} in the beginning of the voyage (8–12 February), when the icebreaker travelled in the Subantarctic open ocean. The peak of SW went down to 300–600 W m^{-2}, when the icebreaker sailed through the MIZ (Fig. 5d). When averaged over daily basis, the daily mean SW was merely around 200–250 W m^{-2}, which was about three times weaker than the diurnal maximum. The diurnal variability in Q_{net} is dominated by SW (Fig. 5f).

Daily mean time series of reanalysed fluxes were constructed at the ship measurement location by linearly interpolating the values at the nearest grid box around the measurement site. Although the ship-based time series is gappy because of missing data, the main features of the ship-reanalysis comparison are clearly shown. The daily mean reanalysis fluxes compare surprisingly well with daily mean ship-based fluxes in the Subantarctic open water, but are significantly underestimated within the MIZ (i.e., the days marked by a solid magenta line in Fig. 5b–d). The ship-based fluxes show that LH and, particularly, SH, enhanced dramatically as

the ship entered the MIZ of February–March on 20 February. The ship-based SH went up to 200 W m^{-2} and LH peaked at 100 W m^{-2} on 27 February. Only MERRA LH and SH have a similar magnitude to ship-based fluxes during 20–23 February; the other reanalyses fluxes are all much weaker. For 24–28 February, the four reanalysed SH values range between 0 and 30 W m^{-2} and reanalysed LH is between 10 and 50 W m^{-2}, both of which are considerably lower than the corresponding ship-based fluxes. As a result, the reanalysed net heat loss from the MIZ is about 100 W m^{-2} less than the ship-based Q_{net} for 27 February (Fig. 5f). It appears that reanalysed fluxes and ship-based fluxes have a reasonable agreement in the Subantarctic regime, but they differ considerably in the MIZ regime.

Latitudinal variations of surface meteorological conditions

Air–sea radiative and turbulent heat exchanges have different characteristics between open water and the marginal ice regions because of the sea-ice modification on the thermodynamic properties of the surface (e.g., albedo, roughness, temperature) and subsequently on air–sea variables and heat exchanges. The air–sea variable measurements provided by the ship included wind speed (W), air temperature (T_a), sea-surface temperature (T_s) and specific humidity (q_a). Latitudinal distributions of the mean conditions of these measured variables and the corresponding reanalysed variables that were collocated with ship measurements are shown (Fig. 6a–d). Wind speed peaked at around 55°S, which is the location of the ACC. Wind speed dropped sharply across 55°S, the outer edge of the MIZ, and remained weak inside the MIZ, but it strengthened again near the Antarctic continent (Fig. 6a). The reanalyses all do well in producing the latitudinal variations of the observed wind speed, except for the very high latitudes near the continent, where the reanalysed wind speeds are weaker.

The thermodynamical variables—q_a, T_s and T_a—all decreased with increasing latitude (Fig. 6b–d), and so the near-surface air in the MIZ was much colder and drier compared to the air over the Subantarctic open ocean. The poleward decrease of q_a is produced by all reanalyses, although the magnitude varies. ERA-interim q_a is slightly drier (i.e., q_a is lower) and NCEP1 q_a is slightly wetter. The reanalyses also produce well the latitudinal changes in observed sea surface temperature (T_s) in the Subantarctic regime, but deviate from observations in the MIZ except for ERA-interim. The ERA-interim T_s shows a high-level consistency with the observed T_s at all latitudes in both the MIZ and Subantarctic regimes. T_s from the other three reanalyses compares poorly with the observed T_s, as it is much colder and also far below the seawater freezing temperature (−1.8°C). One plausible explanation for the extremely cold T_s could be that CFSR and MERRA may use a SIC-weighted approach to blend the ice-surface and sea surface temperatures in assigning T_s in the MIZ. NCEP1 has no mixed sea-ice grids, as it imposes a 55% cut-off threshold. All reanalyses do well in producing the change of T_a at all latitudes, although NCEP1 T_a is slightly colder than all others.

The air–sea differences in humidity and temperature (Fig. 6) feature a U-shape variation with latitude, larger at the two ends of the ship track (i.e., north of the ACC and the MIZ) and weaker in region of the ACC. ERA-interim appears to be a better reanalysis in capturing the observed air–sea conditions over both open water and the mixed sea-ice surface. The other three reanalyses deviate from the observations in varying degrees. It seems that T_s is the main cause of bias in q_s–q_a and T_s–T_a in the MIZ, which gives rise to a large underestimation bias in CFSR, MERRA and NCEP1.

Latitudinal variations of air–sea radiative and turbulent heat fluxes

Latitudinal distributions of the seven-month mean radiative heat flux, including SW↓, SW↑, LW↓ and LW↑ components, and turbulent LH and SH fluxes are shown (Fig. 7). Ship-observed SW↓ showed only a slight poleward reduction (Fig. 7a), while the ship-based SW↑ was highly regime dependent (Fig. 7c). SW↑ was small and barely changed with latitude in the Subantarctic open water, but had a strong poleward increase in the MIZ due to the sea-ice effect on albedo. The sum of SW↓ and SW↑ resulted in a net downward SW that decreased poleward from Hobart near 42°S to the edge of the Antarctic continent at about 68°S (Fig. 7e). The reanalyses generally overestimate both SW↓ and SW↑. The overestimation biases are most evident in the MIZ regime (ca. 58°S), where reanalysed SW↓ is about 30–50 W m^{-2} stronger, and reanalysed SW↑ component is about 10–50 W m^{-2} stronger when compared to ship values. The resultant net downward SW in reanalyses is mostly overestimated (i.e., warm bias) near the outer edge of the MIZ between 65 and 55°S (Fig. 7e).

Ship-based LW↓ and LW↑ both featured a near-linear poleward reduction (Fig. 7b, e). The net LW↑ from the sum of LW↑ and LW↓, however, had little latitudinal variation (Fig. 7f). The two terms have similar rates of poleward reduction, and the latitudinal variations counterbalance each other when the terms are summed up. The reanalyses show a coherent underestimation bias in LW↓ at all latitudes, although they do well for the LW↑

Citation: *Polar Research* 2019, *38*, 3349, http://dx.doi.org/10.33265/polar.v38.3349

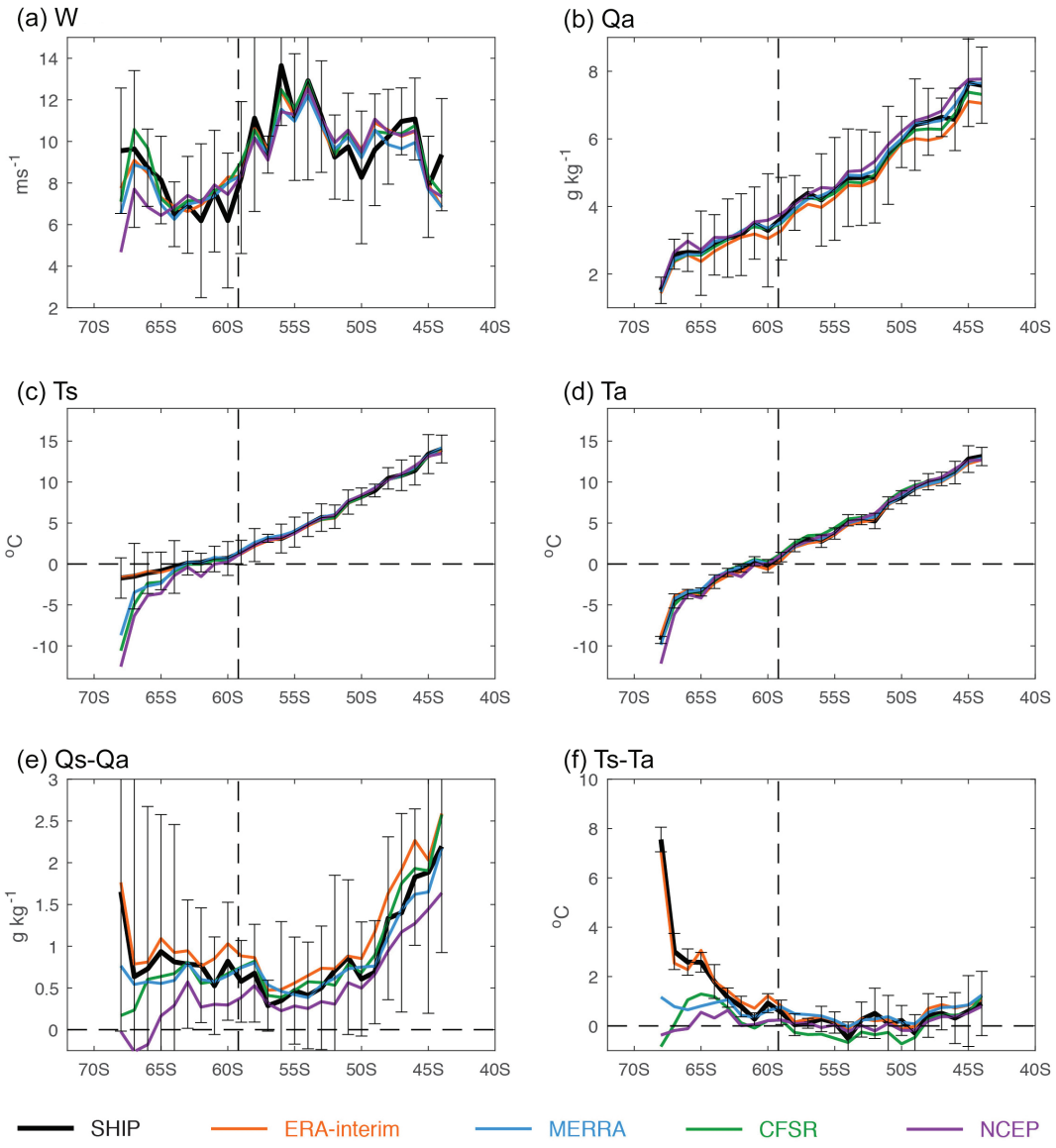

Fig. 6 Latitudinal distributions of air–sea variables from collocated ship and reanalyses averaged over the seven-month period (October–April): (a) W, (b) q_a, (c) T_s, (d) T_a, (e) q_s–q_a and (f) T_s–T_a. Dashed vertical line denotes the seasonal MIZ extent. Error bars indicate 1 SD across ship-based measurements binned at one-degree grids.

component, except for a few latitude degrees off the continent. The bias in LW↓ is so dominant that it gives rise to an overestimation bias (i.e., cold bias) in the reanalysed net upward LW (LW↑–LW↓) in both the MIZ and the Subantarctic regimes (Fig. 7f).

Errors in net SW and LW can be caused by different processes. For instance, downward radiative fluxes are affected more by clouds and aerosols in the atmosphere, while the upward radiative fluxes are more dependent on the specified surface state (e.g., sea and ice surface temperatures, and albedo). Figure 6 indicates that most errors in reanalysed net SW and LW come from the downward components. The reanalyses tend to have stronger SW↓ and weaker LW↓, an indication that the reanalysis models may underestimate the cloud amount. This finding is consistent with recent studies (Trenberth & Fasullo 2010; Haynes et al. 2011; Naud et al. 2014), showing that atmospheric models have difficulty in producing the right amount of low- and mid-level clouds in the Southern Hemisphere. Naud et al. (2014) suggested that the deficiency in the reanalyses' cloud amount is most likely caused by shallow cumulus parameterization schemes used in the models.

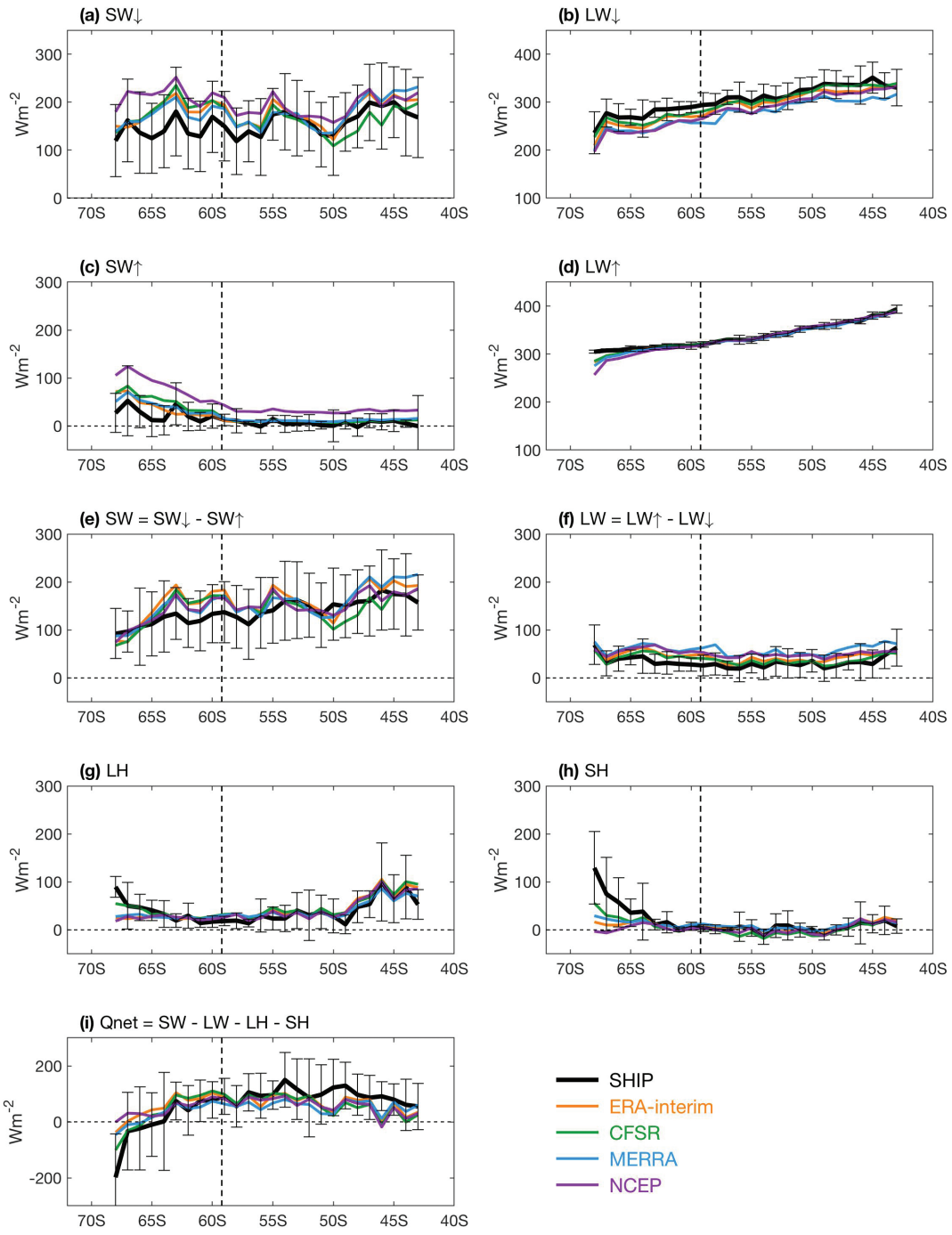

Fig. 7 Latitudinal distributions of surface fluxes from collocated ship and reanalyses averaged over the seven-month analysis period (October–April): (a) SW↓, (b) LW↓, (c) SW↑, (d) upward LW↑, (e) net SW = SW↓–SW↑), (f) net LW (= LW↑–LW↓), (g) turbulent LH flux, (h) turbulent SH, and (i) net heat flux Q_{net} (sum of SW, LW, LH and SH). Dashed vertical lines denote the seasonal MIZ extent. Error bars indicate one SD across all data that are used in constructing the seven-month mean of ship-based fluxes at each one-degree grid point.

Latitudinal variations of turbulent LH and SH fluxes are largely dictated by those of air–sea differences in humidity and temperature, q_s–q_a and T_s–T_a, respectively (Fig. 6e–f). Enhanced LH and SH are shown at the two ends of the ship track, that is, north of the ACC and the MIZ, both of which are the main feature of q_s–q_a and T_s–T_a. Over the Subantarctic, reanalyses slightly overestimate LH heat loss, and this is most evident near the outer edge of the

Citation: *Polar Research* 2019, *38*, 3349, http://dx.doi.org/10.33265/polar.v38.3349

MIZ (ca. 58°S) and at the Subantarctic latitudes between 50 and 45°S. Meanwhile, SH is weak, near zero, in both ship and reanalyses. The reanalysed SH is slightly negative at latitudes between 56 and 48°S. A negative SH indicates that the air is warmer than the ocean surface during the austral summer so that the SH flux is downward to warm up the ocean. As expected, reanalysed LH and SH are generally weaker than ship fluxes in the MIZ because of the weaker air–sea contrasts in the models. However, the bias in LH and SH is not linearly related to the bias in q_s–q_a and T_s–T_a in the MIZ. For instance, ERA-interim flux-related variables all agree well with observations (Fig. 6), but ERA-interim SH is considerably lower than ship SH in the MIZ (Fig. 7g). On the contrary, CFSR T_s–T_a is least comparable with observations (Fig. 6f), but CFSR SH is better produced in sea-ice conditions. In the Subantarctic open water regime, the bias propagation from T_s–T_a to SH is rather direct. The non-linear correlation between flux-related variables and fluxes in the MIZ might be related to the use of different flux algorithms in the mixed sea-ice surfaces in the underlying models (Table 3).

The mean and RMS differences between reanalysed and ship-based fluxes are summarized in Table 4. The statistical properties are listed separately for the MIZ and Subantarctic regimes to show the effect of sea ice on the sign of biases. One marked feature in Table 4 is that the agreement between the four reanalyses (Figs. 2, 3) does not mean that the reanalyses are convergent to a "truth."

Table 4 Mean and RMS differences of reanalysis-minus-ship fluxes for the respective MIZ and Subantarctic regimes.

Regime	Flux	Product	ERA-interim	CFSR	MERRA	NCEP1
MIZ (68–58°S)	SW	DIFF	21	15	11	11
		RMS	36	34	26	26
	LW	DIFF	14	8	24	19
		RMS	18	17	28	27
	LH	DIFF	−4	6	−2	−6
		RMS	20	12	19	22
	SH	DIFF	−23	−17	−20	−32
		RMS	46	27	40	54
	Q_{net}	DIFF	35	18	10	30
		RMS	54	27	48	67
Subantarctic (58–43°S)	SW	DIFF	15	−1	14	6
		RMS	19	19	19	14
	LW	DIFF	11	8	26	18
		RMS	12	10	27	19
	LH	DIFF	10	11	4	6
		RMS	14	14	9	12
	SH	DIFF	2	−6	3	−4
		RMS	6	9	6	8
	Q_{net}	DIFF	−8	−13	−19	−14
		RMS	25	32	30	28

On the contrary, this agreement between products is indicative of a consistent bias. The most pronounced biases include (1) an overestimation of downward SW heating at all latitudes (except for CFSR) by 6–21 W m^{-2}, (2) an overestimation of upward LW cooling at all latitudes by 8–26 W m^{-2}, (3) an overestimation of LH loss in the Subantarctic by 4–11 W m^{-2} and (4) an underestimation of SH loss in the MIZ by 17–32 W m^{-2}. As a result, the surface thermal forcing has a cooling bias (an underestimation of Q_{net}) of 8–19 W m^{-2} over the ice-free water and a warming bias (an overestimation of Q_{net}) of 10–35 W m^{-2} in the sea-ice zone.

A ubiquitous feature of SW at high latitudes in summer

The orientation of Earth's axis to the Sun changes throughout the year, and the change causes a seasonal variation in the intensity (or the zenith angle) of solar radiation reaching the surface and also in the length of day (i.e., number of hours of daylight). The seasonally varying pattern of insolation is the reason that higher latitudes receive less cumulative incoming solar

Table 5 Mean, mean and RMS differences of reanalysis-minus-ship surface meteorological variables for the respective MIZ and Subantarctic regimes.

Regime	Flux	Product	ERAi	CFSR	MERRA	NCEP1
MIZ (68–58°S)	W	MEAN	7.7	8.0	7.5	7.1
		DIFF	−0.1	0.2	−0.3	−0.7
		RMS	1.0	1.2	1.2	1.9
	T_a	MEAN	−2.5	−2.3	−2.2	−2.9
		DIFF	−0.1	0.1	0.2	−0.6
		RMS	0.5	0.4	0.3	1.1
	q_a	MEAN	2.7	2.9	2.9	3.0
		DIFF	−0.2	−0.0	−0.0	0.1
		RMS	0.2	0.10	0.1	0.2
	T_s	MEAN	−0.3	−1.9	−1.5	−2.8
		DIFF	−0.1	−1.6	−1.2	−2.6
		RMS	0.1	3.1	2.4	4.0
Subantarctic (58–43°S)	W	MEAN	10.3	10.3	9.9	10.2
		DIFF	−0.1	−0.1	−0.5	−0.2
		RMS	1.0	0.8	1.1	1.0
	T_a	MEAN	7.1	7.7	7.3	7.5
		DIFF	−0.2	0.3	−0.1	0.1
		RMS	0.3	0.4	0.3	0.4
	q_a	MEAN	5.3	5.5	5.7	5.9
		DIFF	−0.3	−0.1	0.1	0.2
		RMS	0.4	0.2	0.2	0.3
	T_s	MEAN	7.5	7.6	7.7	7.6
		DIFF	−0.1	−0.1	0.2	0.0
		RMS	0.2	0.1	0.2	0.3

radiation than lower latitudes over the course of the year. However, focusing on the summer season, we find that the insolation at high latitudes actually increases towards the South Pole because of the dominance of the length-of-day effect (e.g., Serreze & Barry 2005; Pidwirny 2006). This seemingly counter-intuitive theoretical prediction was examined in a recent study by Grachev et al. (2018), using hourly averaged multiyear data sets collected at two Arctic terrestrial stations that are situated at significantly different latitudes (80.0 and 71.6°N). The study confirmed that the higher latitude site generally receives more total daily amount of the incoming SW and net radiation throughout the summer months than the lower latitude site.

The shipboard measurements used in this study included were gappy on a daily basis, which hindered an examination of seasonal variations in daily mean solar radiation. An attempt was made here to analyse the latitudinal variations of the surface radiation components using the area averaged monthly means (Fig. 8). This approach can provide only a first-order estimation of the variation of surface radiation in different southern latitudes. Nonetheless, given the limited observations in the southern high latitudes, any information derived from ship-based measurements would be helpful for understanding the surface energy budget balance in the off-winter seasons.

We found that the theoretical prediction of poleward increase of SW↓ was not supported when comparing the SW↓ averaged in the MIZ with that in the Subantarctic regime. One plausible explanation for the mismatch between theory and observations might be the large latitudinal gradient between the two areas. SW↓ at a given latitude is governed by both solar zenith angle and the length of day. In the Southern Hemisphere summer, the increase of SW↓ towards the pole occurs only at latitudes where the effect of the length-of-day is sufficiently strong to reverse the latitudinal decreasing tendency associated with solar zenith angle. The zonal average of the global incoming radiation at the top-of-atmosphere observed by the satellite Clouds and the Earth's Radiant Energy System (Kato et al. 2013) suggests that the reversal latitude occurs at about 60° latitude in the Southern Hemisphere.

The edge of the seasonal Antarctic MIZ in our study region is at 58°S. Hence, the SW↓ averaged within the MIZ (68–60°S) was compared with that at the outer edge of the MIZ (59–57°S). We found that the predicted scenario worked for these latitudes (Fig. 8a). Area averages were used to reduce the uncertainty in measurements. The observed SW↓ at the edge of the MIZ was about 15–20 W m^{-2} less than the SW↓ within the MIZ throughout the three summer months, from November to January. From February and onward, there was barely any difference in SW↓ between the two area averaged values.

The poleward increase of SW↓ across the MIZ is well simulated in ERA-interim and MERRA, but only partially produced in CFSR and NCEP. The reanalyses differ from ship measurements in latitudinal gradient of SW↓ between the MIZ (68–60°S) and the Subantarctic (56–42°S) (Fig. 8). While the observed SW↓ in the MIZ (68–60°S) is lower than SW↓ in the Subantarctic (56–42°S) throughout the entire seven-month period, the reanalyses suggest that this occurs only after January/February.

The observed net downward surface radiation SW–LW (the sum of all radiative components expressed as [SW↓– SW↑]–[LW↑–LW↓]) (Fig. 8) shows that the MIZ receives a slightly larger net downward radiation in December solstice when the number of hours of daylight is greatest. Except for CFSR, all the reanalyses do well in producing this feature. Interestingly, despite the large differences between ship measurements and reanalyses in depicting the relative strength of SW↓ between the MIZ (68–60°S) and the Subantarctic (56–42°S), all the reanalyses agree with ship values in showing that the Subantarctic receives more net downward radiation than the MIZ during all seven months. It seems that error compensation between various radiative components is a major problem in the reanalyses.

Seasonal variability of air–sea fluxes

Inter-monthly flux variability was quantified using SD of monthly mean fluxes (Fig. 9a–i). Ship-based observations showed that both SD SW↓ and LW↓ decreased poleward in the Subantarctic regime, but kept nearly steady once inside of the MIZ (Fig.9a, b). SD SW↑ had a large poleward increase in the MIZ, while SD LW↑ was weak and invariant across all latitudes (Fig. 9c, d). The reanalysed SD SW and LW deviate considerably from shipboard observed variances (Fig. 8e, f). In the MIZ, the reanalysed SD SW tends to be higher than observed variainces. In the Subantarctic regime, SD LW and SD SW both tend to be low. The biases in SW and LW may be associated with the parameterization of high-latitude cloud radiative processes in the reanalysis models. Walsh et al. (2009) showed that the reanalysis models simulate the radiative fluxes well if/when the cloud fraction is produced correctly.

Ship-based SD LH (Fig. 9g) showed a rapid reduction poleward, from ca. 70 W m^{-2} near Hobart (45°S) to ca. 10 W m^{-2} on the outer edge of the MIZ (58°S). Once in the MIZ, SD LH increases slightly towards the Antarctic continent, reaching up to 20 W m^{-2} near 68°S. Ship-based SD

Citation: *Polar Research* 2019, *38*, 3349, http://dx.doi.org/10.33265/polar.v38.3349

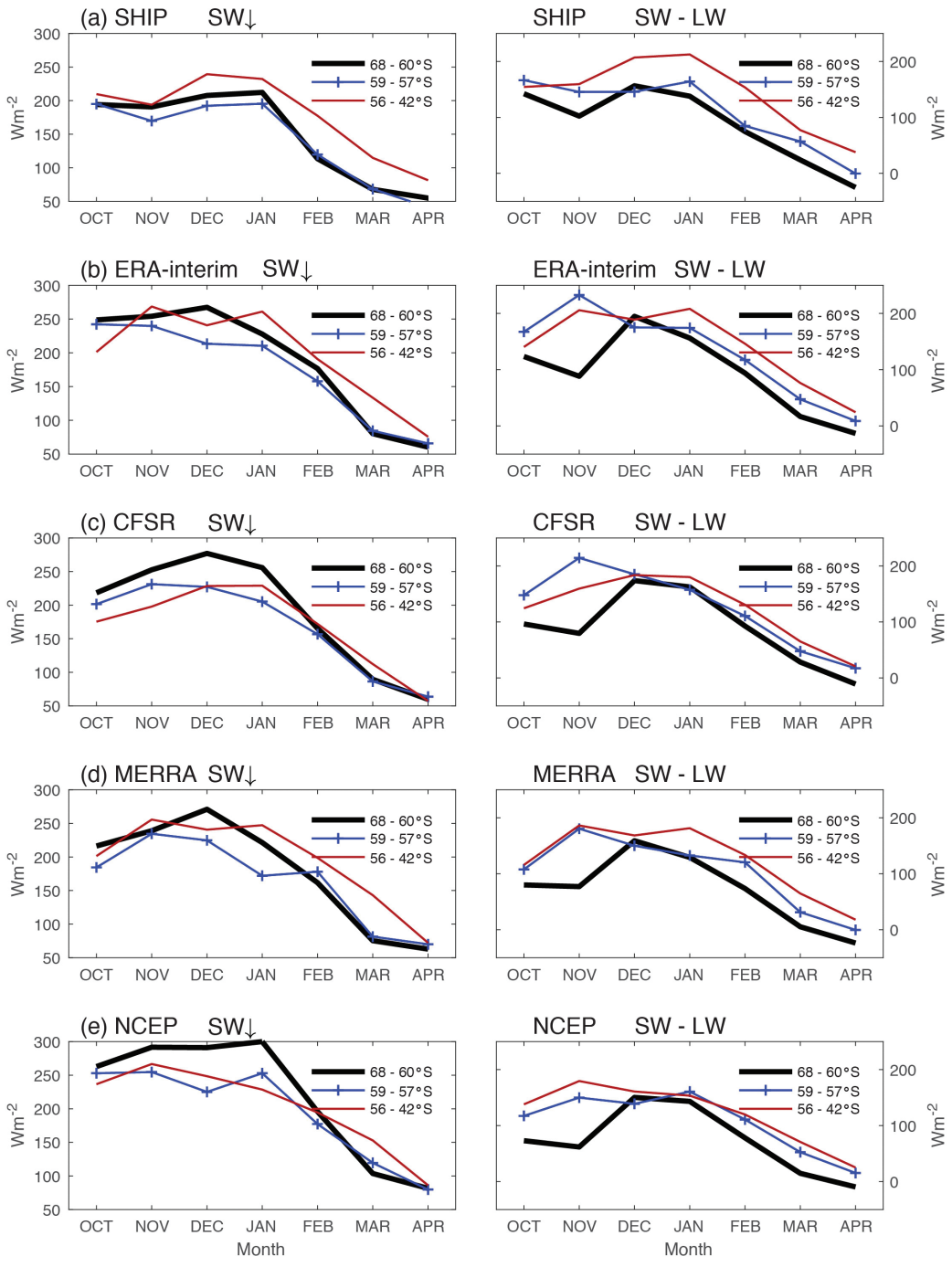

Fig. 8 Seasonal variations of SW↓ (left column) and net SW (= SW↓–SW↑) (right column) averaged over three latitude bands: inside of the MIZ (68–60°S) (thick black line), the outer edge of the MIZ (59–57°S) (blue line with plus sign), and the Subantarctic open water (56–42°S) (red line) constructed from (a) ship observations, (b) ERA-interim, (c) CFSR, (d) MERRA and (e) NCEP1.

SH had, however, a large variability in the MIZ and weak variability in the Subantarctic regime (Fig. 9h). CFSR SD LH and SH have the best agreement with the observed variances, while the SD LH and SH in the other three reanalyses are slightly weaker. LH and SH are usually weak at high latitudes (Yu et al. 2017) because air temperature is usually low. The atmospheric water-holding capacity decreases exponentially with decreasing temperature according to the

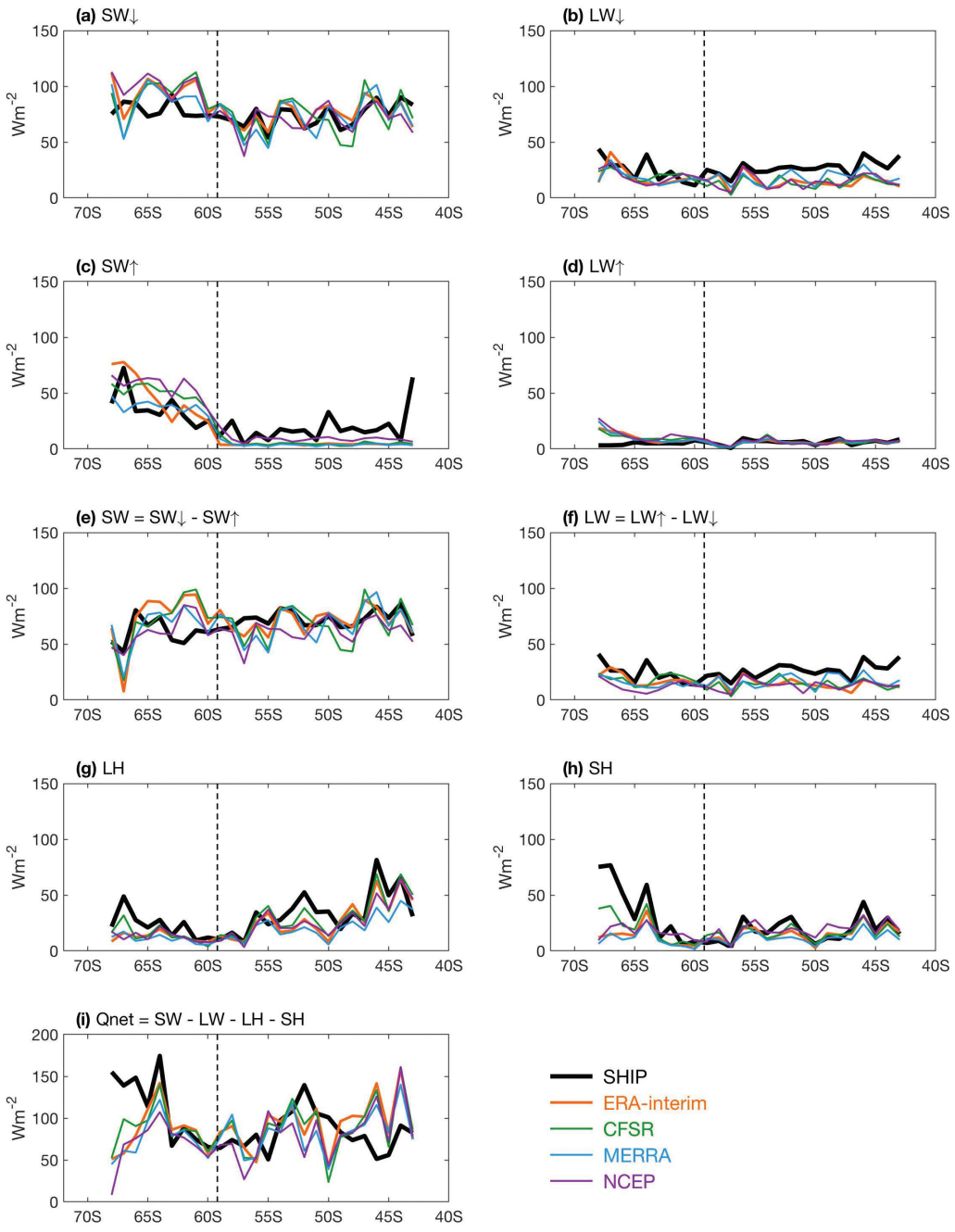

Fig. 9 Latitudinal distributions of the SD of monthly surface fluxes constructed from the seven-month analysis period (October–April). (a) SW↓, (b) LW↓, (c) SW↑, (d) LW↑, (e) net SW (= SW↓–SW↑), (f) net LW (= LW↑–LW↓), (g) turbulent LH flux, (h) turbulent SH flux, and (i) net heat flux Q_{net} (sum of SW, LW, LH and SH). Dashed vertical lines denote the seasonal MIZ extent.

Clausius–Clapeyron equation, which results in low humidity at low temperatures and reduced sea-air thermal heat transfer. On the contrary, SW and LW are highly dependent on latitude, season and clouds (Kato et al. 2013), and so are more variable across the ship tracks from Hobart to the Antarctic MIZ. Although the reanalyses do not have one-to-one correspondence with ship-based SD Q_{net}, general characteristics of the change is represented (Fig. 9i). The reanalyses are consistent in showing that the SD Q_{net} decreases from 42°S to the edge of the MIZ at 58°S, but once in the MIZ, reanalyses deviate from the ship-based SD Q_{net}.

Citation: *Polar Research* 2019, *38*, 3349, http://dx.doi.org/10.33265/polar.v38.3349

Surface heat budget associated with seasonal transitions

Month-to-month variations of surface heat flux components and the net total averaged in the MIZ (68–58°S) and the Subantarctic (58–43°S) are shown (Fig. 10). The net downward solar heating (SW) was the most dominant term both inside and outside of the MIZ during the seven-month off-winter period. SW reached a seasonal high in January (summer) and a low in April (fall). The ship-based SW suggests that SW in the MIZ is about 40–50 W m^{-2} lower than that over the Subantarctic. The SW differences between the two regimes are attributable to both the latitudinal dependence of the solar zenith angle and the influence of albedo and cloudiness. The reanalyses overestimate SW in the MIZ in all months, and the overestimation is largest (ca. 50 W m^{-2}) between October and February. The SW overestimation is also noted in the Subantarctic latitudes, albeit with a lesser degree.

The three surface heat loss terms—LW, LH and SH—are the main mechanisms for returning the solar radiation received at the ocean surface back to the atmosphere. The three flux components showed a vastly different seasonal behaviour with versus without sea ice. In the MIZ (Fig. 10a), increases of the three fluxes started in January (summer), coinciding with the seasonal decline of SW. Ship-based SH showed a rapid enhancement during the summer-to-fall transition, from near zero in January to ca. 60 W m^{-2} in April. Meanwhile, LH and LW each increased by ca. 30 W m^{-2}. The combined turbulent and radiative heat loss quickly offsets the heat gain from SW, turning the MIZ into a heat loss regime in February. The reanalysed LH and SH have a similar increase during this seasonal transition, but the magnitude (<20 W m^{-2}) is about three times weaker. Similarly, the reanalysed LW also has a weak seasonal variation. Despite the differences, reanalyses are consistent in showing that the heat loss in the sea-ice regime started in March, which lags behind the shipboard observations by one month.

The surface heat balance in the Subantarctic open-water regime (Fig. 10b) shows that reanalyses have produced the seasonal variations in individual flux terms. There is a good agreement in SW and SH, but the heat loss by LH and LW are overestimated for all months and in all reanalyses. The predominant cold bias in LW and LH produces a persistent cold bias in the surface heat balance (Q_{net}) by 10–30 W m^{-2} over the seven-month period. The reanalyses suggest that the heat loss over the open water at lower latitudes starts to develop in March, about one month ahead of the ship-based heat budget.

Ship measurements used in this study do not cover the winter season. The wintertime surface energy budget in the MIZ could be learnt from the field programme conducted in the Arctic. A recent study by Walden et al. (2017) reported the seasonal transition of the surface energy budget from winter to summer over young, thin Arctic sea ice, using measurements obtained during the Norwegian Young Sea Ice campaign from January to June of 2015. They found that there was a net heat loss (i.e., the sum of radiative and turbulent heat fluxes is negative) of (–60 to 0 W m^{-2}) in winter due to large heat loss of the net LW flux. From winter to summer, the total net heat budget increased towards positive values of up to nearly 60 W m^{-2}) because of the significant contribution of solar radiation. During spring and summer, the heat loss induced by SH flux was typically between 0 and 20 W m^{-2}, which is comparable to the values in October–December (spring–summer) obtained in this study (Fig. 9a).

Regime-dependent biases in reanalysed surface fluxes

Bias compensation is ubiquitous in all the reanalyses, and this affects the bias characteristics in the total net surface heat budget (Q_{net}) in different regimes. To see the effect more clearly, the seven-month mean regime averaged flux components and the net total were constructed and the differences between reanalysis fluxes and the ship-based fluxes were computed. Estimates of the surface heat balance for each regime are summarized in a schematic manner in Figs. 11 and 12. It is worth mentioning that the reanalysis-minus-ship differences far exceed the uncertainty of the ship-based fluxes. The ship-based SW measurements have an uncertainty of 3 W m^{-2} (RMS 42 W m^{-2}), LW −0.3 W m^{-2} (RMS 11 W m^{-2}), SH −1 W m^{-2} (RMS 9 W m^{-2}) and LH −5 W m^{-2} (RMS 12 W m^{-2}) (Schulz et al. 2012).

In the MIZ (Fig. 11a), reanalysed SW, LW and SH are biased in the same direction. The overestimation bias in SW largely cancels out the overestimation bias in LW, leaving the underestimated SH to dictate the bias in the total heat budget. As a result of the weaker SH loss, the reanalyses all have an excessive net heat input (warm bias) into the MIZ. Over the seven-month period, the ship-based Q_{net} showed a small heat gain, about 16±77 W m^{-2} (Fig. 11b). The warm bias in the reanalyses ranges from 10 W m^{-2} (MERRA) to 36 W m^{-2} (ERA-interim) (see also Table 4), which is about 80–220% of the ship-based Q_{net} value. ERA-interim overestimates the heat gain in the MIZ by twofold.

In the Subantarctic open ocean (Fig. 12a), the SW overestimation bias in the reanalyses is reduced while the LW overestimation bias still persists. The SH bias is small because SH is small, but the LH bias stands

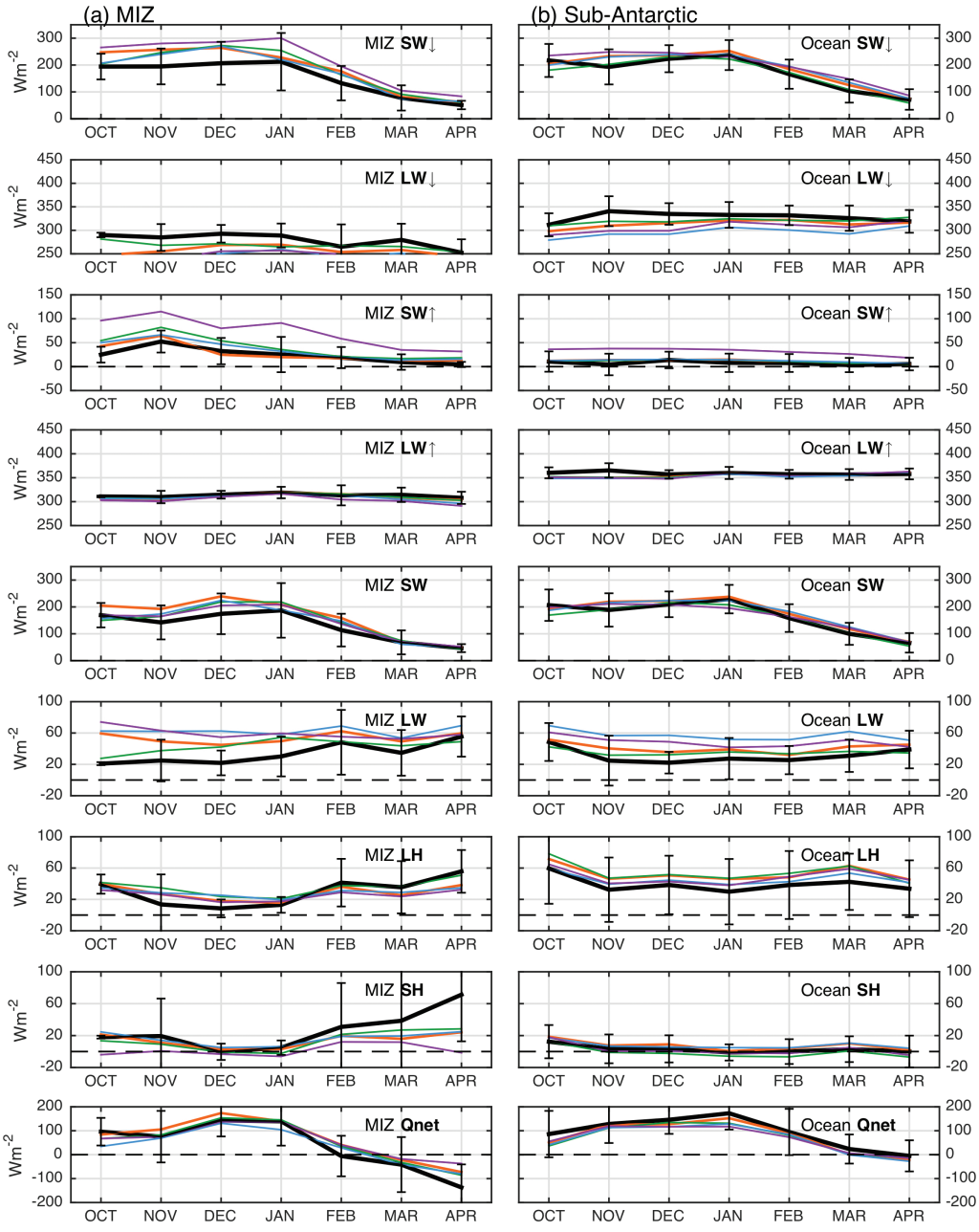

Fig. 10 Top to bottom: seasonal variations of SW↓, LW↓, SW↑, LW↑, net SW (= SW↓–SW↑), net LW (= LW↑–LW↓), turbulent LH flux, turbulent SH flux, and net heat flux Q_{net} (sum of SW, LW, LH and SH) in (a) the seasonal MIZ (68–58°S) and (b) the Subantarctic open ocean (58–42°S). Note that the *y*-axis scale varies with flux components. Error bars indicate the SD differences between the data used in computing the monthly mean of ship-based fluxes.

out. The overestimated LH offsets much of the overestimated SW, causing the LW bias to be the leading source of bias in the total heat budget. Because of the larger radiative cooling by LW, the reanalyses underestimates the total heat gain (cold bias) in the open ocean. The ship-based ocean-surface net heat gain was about 82 ± 78 W m^{-2} (Fig.12b), and the cold bias in the reanalyses ranges from –6 W m^{-2} (ERA-interim) to –20 W m^{-2} (MERRA) (Table 4), accounting for 7–25% of the mean. It appears that the consistency among reanalysed fluxes does not mean the fluxes are correctly determined; rather it reveals a consistent bias when compared to fluxes calculated from shipboard observations.

Citation: *Polar Research* 2019, *38*, 3349, http://dx.doi.org/10.33265/polar.v38.3349

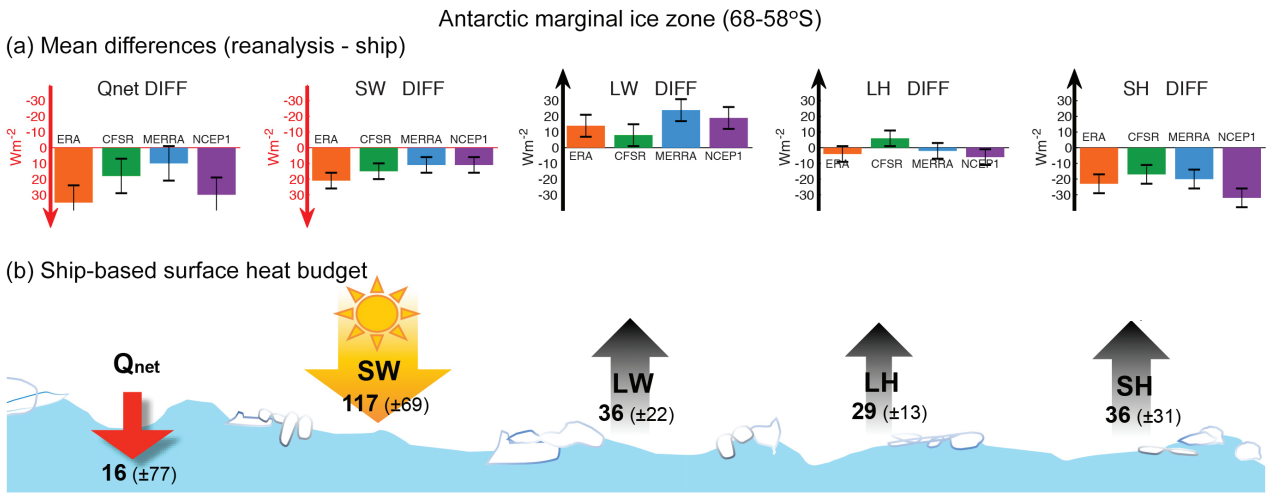

Fig. 11 (a) Left to right: bar plots of the mean difference between reanalysis (RA) and ship in Q_{net}, SW, LW, LH and SH averaged over the Antarctic MIZ. (b) Left to right: ship-based mean flux in Q_{net}, SW, LW, LH and SH in the MIZ. Error bars represent one SD for the measurement points used in constructing the mean. The *x* axis in (a) denotes the products, and the *y* axis denotes the mean difference, with the direction of the axis consistent with the direction of the mean flux defined in (b). Downward fluxes (warm coloured arrows) indicate oceanic heat gain and upward fluxes (black arrows) oceanic heat loss. Positive biases in Q_{net} and SW denote that downward net heat and net SW↓ into the ocean are overestimated (warm bias) and negative biases in Q_{net} and SW denote that downwardnet heat and net SW↓ into the ocean are underestimated (cold bias).

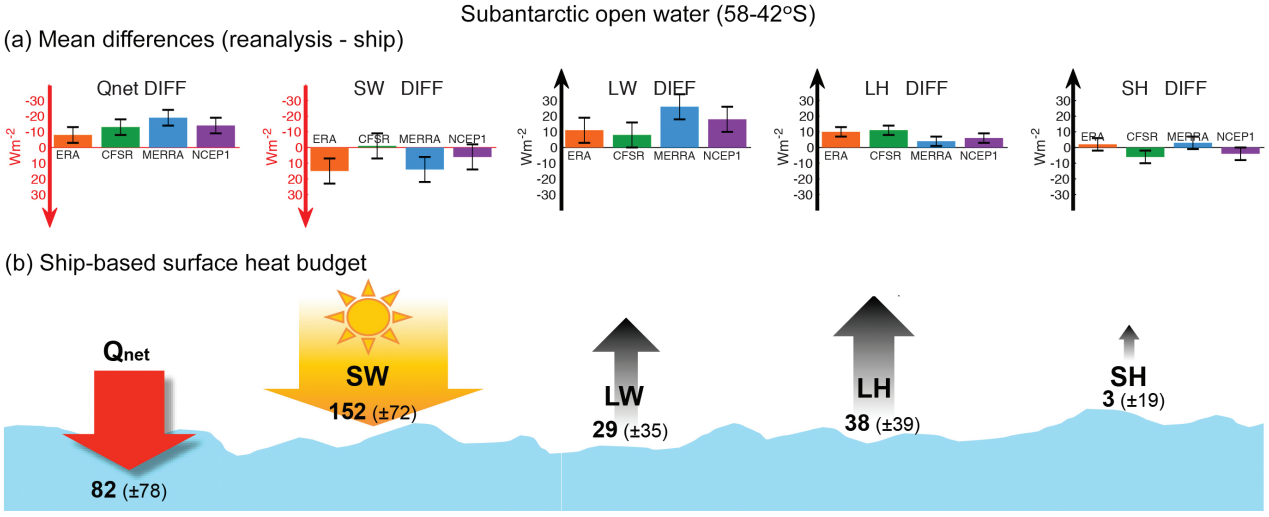

Fig. 12 (a) Left to right: bar plots of the mean difference between reanalysis (RA) and ship in Q_{net}, SW, LW, LH and SH averaged over the Southern Ocean. (b) Left to right: ship-based mean flux in Q_{net}, SW, LW, LH and SH in the MIZ. Error bars represent one SD for the measurement points used in constructing the mean. The *x* axis in (a) denotes the products, and the *y* axis denotes the mean difference, with the direction of the axis consistent with the direction of the mean flux defined in (b). Downward fluxes (warm coloured arrows) indicate oceanic heat gain and upward fluxes (black arrows) oceanic heat loss. Positive biases in Q_{net} and SW denote that downward net heat and net SW↓ into the ocean are overestimated (warm bias) and negative biases in Q_{net} and SW denote that downward-net heat and net SW↓ into the ocean are underestimated (cold bias).

Summary

The Southern Ocean surface heat fluxes from four atmospheric reanalyses—CFSR, ERA-interim, MERRA and NCEP1—were evaluated using air–sea measurements obtained from the icebreaker *Aurora Australis* during off-winter seasons in 2010–12. The icebreaker tracked between Hobart (ca. 42°S), and the Antarctic continent,

providing in situ benchmark observations pertinent to the surface energy budget change in two regimes: the Subantarctic Southern Ocean (58–42°S) and the eastern Antarctic MIZ (68–58°S). It is worth noting that the ship-based fluxes do not really represent measured fluxes; rather they were obtained using bulk parameterizations with ship-measured surface meteorological variables as input. The study used the COARE algorithm for the fluxes over the ice-free Subantarctic regime and the SHEBA algorithm for the fluxes over the MIZ. The four reanalyses have different approaches to treat the grids in the sea-ice zone and also different algorithms for the Subantarctic open ocean.

The reanalyses show a high-level agreement among themselves, but this agreement reflects a universal bias, not a "truth." SW↓ is overestimated (warm biased) and LW↓ is underestimated (cold biased), an indication that the cloud amount in all the models is too low. The ocean surface in both regimes shows a heat gain from the atmosphere when averaged over the seven months (October–April). However, the ocean heat gain in the reanalyses is overestimated by 10–36 W m^{-2} (80–220%) in the MIZ but underestimated by 6–20 W m^{-2} (7–25%) in the Subantarctic. The biases in SW↓ and LW↓ cancel out each other in the MIZ, and the main error contributor is the underestimated SH loss caused by weak air–sea temperature gradients in the models. In the Subantarctic regime, the cold bias in LW↓ dominates the total heat budget.

In summary, two biases stand out in the reanalyses: the excessive LW cooling across the MIZ and the Subantarctic open water and the weak heat loss by SH in the MIZ. CFSR shows a slightly better agreement with ship observations compared to the other three reanalyses, perhaps due to the inclusion of an interactive ice model. ERA-interim air–sea variables (near-surface air temperature and humidity, wind speed, etc.) in the MIZ have the best comparison with ship measurements, but this does not translate to a better comparison of the fluxes.

The biases in the reanalyses affect the surface energy budgets in the Southern Ocean in two meaningful ways. One effect is the timing of the seasonal transition from net heat gain to net heat loss at the ocean surface. The reanalyses show that the transition occurs in March for both the Subantarctic and MIZ regimes, while the ship-based surface heat budget suggests that the transition starts in February in the MIZ and April in the Subantarctic ocean. The other effect is the relative strength of SW↓ between the two regimes. The reanalyses show that SW↓ in the higher-latitude MIZ is higher than that in the lower-latitude Subantarctic during the summer months (November–January). By contrast, the ship measurements show that SW↓ in the MIZ in the summer, though higher than SW↓ on the outer edge of the MIZ because of longer hours of sunlight, is always lower than that in the Subantarctic. The surface heat budget is a delicate balance between the heat gain by net downward solar radiation and the heat loss by turbulent heat fluxes and LW. The reanalyses have yet to reproduce this balance.

The high-latitude Southern Ocean represents a smaller area compared to lower latitudes of the Southern Ocean. A large flux bias in the MIZ is relatively less important compared to a similar magnitude flux bias at lower latitudes in a global context. Nevertheless, these flux biases are locally important wherever they occur, as they affect the heat budget estimation and hinder our efforts in contemplating the role of the ocean heat transport in the Southern Ocean climate.

Acknowledgements

Data from the icebreaker *Aurora Australis* are managed by the Australian Integrated Marine Observing System (http://imos.org.au/flux_data.html). NSIDC SIC data were downloaded from https://nsidc.org, ERA-interim data from http://rda.ucar.edu, CFSR data from http://rda.ucar.edu, NCEP1 data from http://www.esrl.noaa.gov/psd/ and MERRA data from http://disc.sci.gsfc.nasa.gov. We thank the late Edgar Andreas for providing the FORTRAN code for the SHEBA algorithm at http://www.nwra.com/resumes/andreas/, and also thank two anonymous reviewers for their comments that have helped improve the presentation of the manuscript.

Disclosure statement

The authors report no conflict of interest.

Funding

The study is supported by the NOAA Climate Observation Division grant NA14OAR4320158 and NOAA Modeling, Analysis, Predictions, and Projections Program's Climate Reanalysis Task Force through grant no. NA13OAR4310106.

References

Alam A. & Curry J. 1995. Lead-induced atmospheric circulations. *Journal of Geophysical Research—Oceans 100*, 4643–4652, http://dx.doi.org/10.1029/94JC02562.

Allison I., Brandt R.E. & Warren S.G. 1993. East Antarctic sea ice: albedo, thickness distribution, and snow cover. *Journal of Geophysical Research—Oceans 98*, 12417–12429, http://dx.doi.org/10.1029/93JC00648.

Allison I., Tivendale C.M. & Akerman G.J., Tann J.M. & Wills R.H. 1982. Seasonal variations in the surface energy exchanges over Antarctic sea ice and coastal waters. *Annals of Glaciology 3*, 12–16, http://dx.doi.org/10.3189/S0260305500002445.

Anderson R.J. 1987. Wind stress measurements over rough ice during the 1984 Marginal Ice Zone Experiment. *Journal of Geophysical Research—Oceans 92*, 6933–6941, http://dx.doi.org/10.1029/JC092iC07p06933.

Andreas E.L. 1987. A theory for the scalar roughness and the scalar transfer coefficients over snow and sea ice. *Boundary-Layer Meteorology 38*, 159–184, http://dx.doi.org/10.1007/BF00121562.

Andreas E.L. 2002. Parameterizing scalar transfer over snow and ice: a review. *Journal of Hydrometeorology 3*, 417–432, http://dx.doi.org/10.1175/1525-7541(2002)003<0417:PSTOSA>2.0.CO;2.

Andreas E.L, Horst T.W., Grachev A.A., Persson P.O.G., Fairall C.W., Guest P.S. & Jordan R.E. 2010. Parameterising turbulent exchange over summer sea ice and the marginal ice zone. *Quarterly Journal of the Royal Meteorological Society 136*, 927–943, http://dx.doi.org/10.1002/qj.618.

Andreas E.L., Paulson C.A., Williams R.M., Lindsay R.W. & Businger J.A. 1979. The turbulent heat flux from Arctic leads. *Boundary Layer Meteorology 17*, 57–91. http://dx.doi.org/10.1007/BF00121937.

Andreas E.L., Persson P., Jordan R.E., Horst T.W., Guest P.S., Grachev A.A. & Fairall C.W. 2010. Parameterizing turbulent exchange over sea ice in winter. *Journal of Hydrometeorology 11*, 87–104, http://dx.doi.org/10.1175/2009JHM1102.1.

Andreas E.L., Tucker W.B. III & Ackley S.F. 1984. Atmospheric boundary-layer modification, drag coefficient, and surface heat flux in the Antarctic marginal ice zone. *Journal of Geophysical Research—Oceans 89*, 649–661, http://dx.doi.org/10.1029/JC089iC01p00649.

Bennett T.J. Jr. & Hunkins K. 1986. Atmospheric boundary layer modification in the marginal ice zone. *Journal of Geophysical Research—Oceans 91*, 13033–13044, http://dx.doi.org/10.1029/JC091iC11p13033.

Birnbaum G. & Lupkes C. 2002. A new parameterization of surface drag in the marginal sea ice zone. *Tellus 54A*, 107–123, http://dx.doi.org/10.1034/j.1600-0870.2002.00243.x.

Brandt R.E., Warren S.G., Worby A.P. & Grenfell T.C. 2005. Surface albedo of the Antarctic sea ice zone. *Journal of Climate 18*, 3606–3622, http://dx.doi.org/10.1175/JCLI3489.1.

Bromwich D.H., Chen B., Hines K.M. & Cullather R.I. 1998. Global atmospheric responses to Antarctic forcing. *Annals of Glaciology 27*, 521–527.

Cerovečki I., Talley L.D. & Mazloff M.R. 2011. A comparison of Southern Ocean air–sea buoyancy flux from an ocean state estimate with five other products. *Journal of Climate 24*, 6283–6306, http://dx.doi.org/10.1175/2011JCLI3858.1.

Comiso J.C. & Zwally H.J. 1984. Concentration gradients and growth/decay characteristics of the seasonal sea ice cover. *Journal of Geophysical Research 89*, 8081–8103, http://dx.doi.org/10.1029/JC089iC05p08081.

Dee D.P., Uppala S.M., Simmons A.J., Berrisford P., Poli P., Kobayashi S., Andrae U., Balmaseda M.A., Balsamo G., Bauer P., Bechtold P., Beljaars A.C.M., van de Berg L., Bidlot J., Bormann B., Delsol C., Dragani R., Fuentes M., Geer A.J., Haimberger L., Healy S.B. Hersbach H., Hólm E.V., Isaksen, L., Kallberg P., Kohler M., Matricardi M., McNally A.P., Monge-Sanz B.;M., Morcrette J.-J., Park B.-K., Peubey C., de Rosnay P., Tavalato C., Thépaut J.-N. & Vitart F. 2011. The ERA-Interim reanalysis: configuration and performance of the data assimilation system. *Quarterly Journal of the Meteorological Society 137*, 553–597, http://dx.doi.org/10.1002/qj.828.

Fairall C.W., Bradley E.F., Hare J.E., Grachev A.A. & Edson J.B. 2003. Bulk parameterization of air–sea fluxes: updates and verification for the COARE algorithm. *Journal of Climate 16*, 571–591, http://dx.doi.org/10.1175/1520-0442(2003)016<0571:BPOASF>2.0.CO;2.

Foken T. 2008. The energy balance closure problem: an overview. *Ecological Applications 18*, 1351–1367, http://dx.doi.org/10.1890/06-0922.1.

Grachev A.A., Andreas E.L., Fairall C.W., Guest P.S. & Persson P.O.G. 2007. SHEBA flux-profile relationships in the stable atmospheric boundary layer. *Boundary-Layer Meteorology 124*, 315–333, http://dx.doi.org/10.1007/s10546-007-9177-6.

Grachev A.A., Persson P.O.G., Uttal T., Akish E.A., Cox C.J., Morris S.M., Fairall C.W., Stone R.S., Lesins G., Makshtas A.P. & Repina I.A. 2018. Seasonal and latitudinal variations of surface fluxes at two Arctic terrestrial sites. *Climate Dynamics 51*, 1793–1818, http://dx.doi.org/10.1007/s00382-017-3983-4.

Guest P.S. & Davidson K.L. 1987. The effect of observed ice conditions on the drag coefficient in the summer East Greenland Sea marginal ice zone. *Journal of Geophysical Research—Oceans 92*, 6943–6954, http://dx.doi.org/10.1029/JC092iC07p06943.

Hastenrath S. 1982. On meridional heat transport in the world ocean. *Journal of Physical Oceanography 12*, 922–927, http://dx.doi.org/10.1175/1520-0485(1982)012<0922:OMHTIT>2.0.CO;2.

Haynes J.M., Jakob C., Rossow W.B., Tselioudis G. & Brown J. 2011. Characteristics of Southern Ocean cloud regimes and their effects on the energy budget. *Journal of Climate 24*, 5061–5080, http://dx.doi.org/10.1175/2011JCLI4052.1.

Hibler W.D. III 1979. A dynamic thermodynamic sea ice model. *Journal of Physical Oceanography 9*, 815–846.

Hill K., Moltmann T., Proctor R. & Allen S. 2010. The Australian Integrated Marine Observing System: delivering data streams to address national and international research priorities. *Marine Technology Society Journal 44*, 65–72, http://dx.doi.org/10.4031/MTSJ.44.6.13.

Hudson D.A. & Hewitson C. 2001. The atmospheric response to a reduction in summer Antarctic sea-ice extent. *Climate Research 16*, 79–99, http://dx.doi.org/10.3354/cr016079.

Hunke E.C. & Dukowicz J.K. 1997. An elastic–viscous–plastic model for sea ice dynamics. *Journal of Physical Oceanography 27*, 1849–1867, http://dx.doi.org/10.1175/1520-0485(1997)027<1849:AEVPMF>2.0.CO;2.

Jacobs A.F.G., Heusinkveld B.G. & Holtslag A.A.M. 2008. Towards closing the surface energy budget of a mid-latitude

grassland. *Boundary-Layer Meteorology 126*, 125–136, http://dx.doi.org/10.1007/s10546-007-9209-2.

Kalnay, E., Kanamitsu M., Kistler R., Collins W., Deaven D., Gandin L., Iredell M., Saha S., White G., Woollen J., Zhu Y., Leetmaa A., Reynolds R., Chelliah M., Ebisuzaki W., Higgins W., Janowiak J., Mo K.C., Ropelewski C., Wang J., Jenne R. & Joseph D. 1996. The NCEP/NCAR 40-year reanalysis project. *Bulletin of the American Meteorological Society 77*, 437–472.

Kato S., Loeb N.G., Rose F.G., Doelling D.R., Rutan D.A., Caldwell T.E., Yu L. & Weller R.A. 2013. Surface irradiances consistent with CERES-derived top-of-atmosphere shortwave and longwave irradiances. *Journal of Climate 26*, 2719–2740, https://doi.org/10.1175/JCLI-D-12-00436.1.

King J.C. & Turner J. 1997. *Antarctic meteorology and climatology*. Cambridge: Cambridge University Press.

Kottmeier C. & Engelbart D. 1992. Generation and atmospheric heat exchange of coastal polynyas in the Weddell Sea. *Boundary Layer Meteorology 60*, 207–234, http://dx.doi.org/10.1007/BF00119376.

Kottmeier C. & Sellmann L. 1996. Atmospheric and oceanic forcing of Weddell Sea ice motion. *Journal of Geophysical Research—Oceans 101*, 20809–20824, http://dx.doi.org/10.1029/96JC01293.

Leuning R., van Gorsel E., Massman W.J. & Isaac P.R. 2012. Reflections on the surface energy imbalance problem. *Agricultural and Forest Meteorology 156*, 65–74, http://dx.doi.org/10.1016/j.agrformet.2011.12.002.

Lupkes C. & Gryanik V.M. 2015. A stability-dependent parametrization of transfer coefficients for momentum and heat over polar sea ice to be used in climate models. *Journal of Geophysical Research—Atmospheres 120*, 552–581, http://dx.doi.org/10.1002/2014JD022418.

McPhee M.G., Ackley S.F., Guest P., Huber B.A., Martinson D.G., Morison J.H., Muench R.D., Padman L. & Stanton T.P. 1996. The Antarctic Zone Flux Experiment. *Bulletin of the American Meteorological Soceity 77*, 1221–1232, http://dx.doi.org/10.1175/1520-0477(1996)077<1221:TAZFE>2.0.CO;2.

McPhee M.G., Maykut G.A. & Morison J.H. 1987. Dynamics and thermodynamics of the ice/upper ocean system in the marginal ice zone of the Greenland Sea. *Journal of Geophysical Research 92*, 7017–7031, http://dx.doi.org/10.1029/JC092iC07p07017.

Manabe S. & Stouffer R.J. 1980. Sensitivity of a global climate model to an increase of CO_2 concentration in the atmosphere. *Journal of Geophysical Research—Oceans 85*, 5529–5554, http://dx.doi.org/10.1029/JC085iC10p05529.

Markus T. & Cavalieri D.J. 2000. An enhancement of the NASA Team sea ice algorithm. *IEEE Transactions on Geoscience and Remote Sensing 38*, 1387–1398, http://dx.doi.org/10.1109/36.843033.

Maykut G.A. & McPhee M.G. 1995. Solar heating of the Arctic mixed layer. *Journal of Geophysical Research—Oceans 100*, 24691–24703, http://dx.doi.org/10.1029/95JC02554.

Meinel A.B. & Meinel M.P. 1976. *Applied solar energy: an introduction*. Reading: Addison Wesley Publishing.

Meyers G. 2008. The Australian integrated marine observing system. *Journal of Ocean Technology 3*, 80–81.

Naud C.M., Booth J.F. & Del Genio A.D. 2014. Evaluation of ERA-Interim and MERRA Cloudiness in the Southern Ocean. *Climate 27*, 2109–2124, http://dx.doi.org/10.1175/JCLI-D-13-00432.1.

Nygard T., Vihma T., Birnbaum G., Hartmann J., King J., Lachlan-Cope T., Ladkin R., Lupkes C. & Weiss A. 2016. Validation of eight atmospheric reanalyses in the Antarctic Peninsula region. *Quarterly Journal of the Royal Meteorological Society 142*, 684–692, http://dx.doi.org/10.1002/qj.2691.

Pedersen C.A., Roeckner E., Lüthje M. & Winther J.-G. 2009. A new sea ice albedo scheme including melt ponds for ECHAM5 general circulation model. *Journal of Geophysical Research—Atmospheres 114*, D08101, https://doi.org/10.1029/2008JD010440.

Pidwirny M. 2006. Earth–sun relationships and insolation. In M. Pidwirny: *Fundamentals of physical geography*. 2nd edn. Accessed on the internet at http://www.physicalgeography.net/fundamentals/6i.html 15 November 2018.

Renfrew I.A., Moore G.W., Guest P.S. & Bumke K. 2002. A comparison of surface layer and surface turbulent flux observations over the Labrador Sea with ECMWF analyses and NCEP reanalyses. *Journal of Physical Oceanography 32*, 383–400, http://dx.doi.org/10.1175/1520-0485(2002)032<0383:ACOSLA>2.0.CO;2.

Rienecker M.M., Suarez M.J., Gelaro R., Todling R., Bacmeister J., Liu E., Bosilovich M.G., Schubert S.D., Takacs L., Kim G., Bloom S., Chen J., Collins D., Conaty A., da Silva A., Gu W., Joiner J., Koster R.D., Lucchesi R., Molod A., Owens T., Pawson S., Pegion P., Redder C.R., Reichle R., Robertson F.R., Ruddick A.G., Sienkiewicz M. & Woollen J. 2011. MERRA: NASA's modern-era retrospective analysis for research and applications. *Journal of Climate 24*, 3624–3648, http://dx.doi.org/10.1175/JCLI-D-11-00015.1.

Rintoul S.R., Hughes C.W. & Olbers D. 2001. The antarctic circumpolar current system. In G. Siedler et al. (eds.): *Ocean circulation and climate*. *Vol. 103*. Pp. 271–302. New York: Academic Press.

Ruffieux D., Persson P.O.G., Fairall C.W. & Wolfe D.W. 1995. Ice pack and lead surface-energy budgets during LEADEX-1992. *Journal of Geophysical Research—Oceans 100*, 4593–4612, http://dx.doi.org/10.1029/94JC02485.

Saha S., Moorthi S., Pan H., Wu X., Wang J., Nadiga S., Tripp P., Kistler R., Woollen J., Behringer D., Liu H., Stokes D., Grumbine R., Gayno G., Wang J., Hou Y., Chuang H., Juang H.H., Sela J., Iredell M., Treadon R., Kleist D., Van Delst P., Keyser D., Derber J., Ek M., Meng J., Wei H., Yang R., Lord S., van den Dool H., Kumar A., Wang W., Long C., Chelliah M., Xue Y., Huang B., Schemm J., Ebisuzaki W., Lin R., Xie P., Chen M., Zhou S., Higgins W., Zou C., Liu Q., Chen Y., Han Y., Cucurull L., Reynolds R.W., Rutledge G. & Goldberg M. 2010. The NCEP climate forecast system reanalysis. *Bulletin of the American Meteorological Society 91*, 1015–1057, http://dx.doi.org/10.1175/2010BAMS3001.1.

Schnell R.C., Barry R.G., Miles M.W., Andreas E.L., Radke L.F., Brock C.A., McCormick M.P. & Moore J.L. 1989. Lidar detection of lead in Arctic sea ice. *Nature 339*, 530–532, http://dx.doi.org/10.1038/339530a0.

Schulz E., Josey S.A. & Verein R. 2012. First air–sea flux mooring measurements in the Southern Ocean. *Geophysical Research Letters 39*, L16606, http://dx.doi.org/10.1029/2012GL052290.

Serreze M.C. & Barry R.G. 2005. *The Arctic climate system*. Cambridge: Cambridge University Press.

Strong C. & Rigor I.G. 2013. Arctic marginal ice zone trending wider in summer and narrower in winter. *Geophysical Research Letter 40*, 4864–4868, https://doi.org/10.1002/grl.50928.

Tetzla A., Lupkes C. & Hartmann J. 2015. Aircraft-based observations of atmospheric boundary-layer modification over Arctic leads. *Quarterly Journal of the Royal Meteorological Society 141*, 2839–2856, http://dx.doi.org/10.1002/qj.2568.

Trenberth K.E. & Fasullo J. 2010. Simulation of present-day and twenty-first-century energy budgets of the Southern Oceans. *Journal of Climate 23*, 440–454, http://dx.doi.org/10.1175/2009JCLI3152.1.

Vihma T. 1995. Subgrid parameterization of surface heat and momentum fluxes over polar oceans. *Journal of Geophysical Research—Oceans 100*, 22625–22646, http://dx.doi.org/10.1029/95JC02498.

Vihma T., Uotila J., Cheng B. & Launiainen J. 2002. Surface heat budget over the Weddell Sea: buoy results and model comparisons. *Journal of Geophysical Research—Oceans 107*, article no. 3013, http://dx.doi.org/10.1029/2000JC000372.

Wadhams P., Squire V.A., Ewing J.A. & Pascal R.W. 1986. The effect of the marginal ice zone on the directional wave spectrum of the ocean. *Journal of Physical Oceanography 16*, 358–376, http://dx.doi.org/10.1175/1520-0485(1986)016<0358:TEOTMI>2.0.CO;2.

Walden V.P., Hudson S.R., Cohen L., Murphy S.Y. & Granskog M.A. 2017. Atmospheric components of the surface energy budget over young sea ice: results from the N-ICE2015 campaign. *Journal of Geophysical Research—Atmospheres 122*, 8427–8446, http://dx.doi.org/10.1002/2016JD026091.

Walsh J.E., Chapman W.L. & Portis D.H. 2009. Arctic cloud fraction and radiative fluxes in atmospheric reanalyses. *Journal of Climate 22*, 2316–2334, https://doi.org/10.1175/2008JCLI2213.1.

Wendler G., Hartmann B., Wyatt C., Shulski M. & Stone H. 2005. Midsummer energy balance for the southern seas. *Boundary Layer Meteorology 117*, 131–148, https://doi.org/10.1007/s10546-004-7090-9.

Wilson K., Goldstein A., Falge E., Aubinet M., Baldocchi D., Berbigier P., Bernhofer C., Ceulemans R., Dolman H., Field C., Grelle A., Ibrom A., Law B.E., Kowalski A., Meyers T., Moncrieff J., Monson R., Oechel W., Tenhunen J., Valentini R. & Verma S., 2002. Energy balance closure at FLUXNET sites. *Agricultural and Forest Meteorology 113*, 223–243, https://doi.org/10.1016/S0168-1923(02)00109-0.

Winton M. 2000. A reformulated three-layer sea ice model. *Journal of Atmospheric and Oceanic Technology 17*, 525–531, https://doi.org/10.1175/1520-0426(2000)017<0525:ARTLSI>2.0.CO;2.

Wu X. & Grumbine R. 2014. Sea ice in the NCEP climate forecast system. *Climate Prediction Se²T Digest. Science and Technology Infusion Climate Bulletin Supplement February 2014*, 28–35.

Yu L. 2019. Global air–sea fluxes of heat, fresh water, and momentum: energy budget closure and unanswered questions. *Annual Review of Marine Science 11*, 227-248, https://doi.org/10.1146/annurev-marine-010816-060704.

Yu L., Jin X., Schulz E. & Josey S.A. 2017. Air–sea interaction regimes in the sub-Antarctic Southern Ocean and Antarctic marginal ice zone revealed by icebreaker measurements. *Journal of Geophysical Research—Oceans 122*, 6547–6564. https://doi.org/10.1002/2016JC012281.

Yu L. & Weller R.A. 2007. Objectively analyzed air–sea heat fluxes for the global ocean-free oceans (1981–2005). *Bulletin of the American Meteorological Society 88*, 527–539, https://doi.org/10.1175/BAMS-88-4-527.

Yuan X.J. & Martinson D.G. 2000. Antarctic sea ice extent variability and its global connectivity. *Journal of Climate 13*, 1697–1717, https://doi.org/10.1175/1520-0442(2000)013<1697:ASIEVA>2.0.CO;2.

Zwally H.J., Comiso J.C., Parkinson C.L., Cavalieri D.J. & Gloersen P. 2002. Variability of Antarctic sea ice 1979–1998. *Journal of Geophysical Research—Oceans 107*, article no. 3041, https://doi.org/10.1029/2000JC000733.